Microvascular Research

https://www.journals.elsevier.com/microvascular-research

ISSN: 0026-2862; Impact factor = 3.514

Accepted July 4th 2021

(extra corrections in purple font)

FINITE ELEMENT COMPUTATION OF MAGNETO-HEMODYNAMIC FLOW AND HEAT TRANSFER IN A BIFURCATED ARTERY WITH SACCULAR ANEURYSM USING THE CARREAU-YASUDA BIORHEOLOGICAL MODEL

Ankita Dubey[1], B. Vasu[1*], O. Anwar Bég[2] and R. S. R. Gorla[3]

[1]*Department of Mathematics, Motilal Nehru National Institute of Technology, Allahabad, Prayagraj-211004,* ***India****.*

[2]*Multi-Physical Engineering Sciences, Aeronautical/Mechanical Engineering, Salford University, M54WT,* ***UK.***

[3]*Departmen of Aeronautics and Astronautics, Air force Institute of Technology, Wright Patterson Air Force Base, Dayton, Ohio,* ***USA****.*

**Corresponding author- email: bvasu@mnnit.ac.in*

ABSTRACT: Existing computational fluid dynamics studies of blood flows have demonstrated that the lower wall stress and higher oscillatory shear index might be the cause of acceleration in atherogenesis of vascular walls in hemodynamics. To prevent the chances of aneurysm wall rupture in the saccular aneurysm at distal aortic bifurcation, clinical biomagnetic studies have shown that extra-corporeal magnetic fields can be deployed to regulate the blood flow. Motivated by these developments, in the current study a finite element computational fluid dynamics simulation has been conducted of unsteady two-dimensional non-Newtonian magneto-hemodynamic heat transfer in electrically conducting blood flow in a bifurcated artery featuring a saccular aneurysm. The fluid flow is assumed to be pulsatile, non-Newtonian and incompressible. The Carreau-Yasuda model is adopted for blood to mimic non-Newtonian characteristics. The transformed equations with appropriate boundary conditions are solved numerically by employing the finite element method with the variational approach in the FreeFEM++ code. Hydrodynamic and thermal characteristics are elucidated in detail for the effects of key non-dimensional parameters i. e. Reynolds number (Re = 14, 21, 100, 200), Prandtl number (Pr = 14, 21) and magnetic body force parameter (Hartmann number) (M = 0.6, 1.2, 1.5) at the aneurysm and throughout the arterial domain. The influence of vessel geometry on blood flow characteristics i. e. velocity, pressure and temperature fields are also visualized through instantaneous contour patterns. It is found that an increase in the magnetic parameter reduces the pressure but increases the skin-friction coefficient in the domain. The temperature decreases at the parent artery (inlet) and both the distant and prior artery with the increment in the Prandtl number. A higher Reynolds number also causes a reduction in velocity as well as in pressure. The blood flow shows different characteristic contours with time variation at the aneurysm as well as in the arterial segment. *The novelty of the current research is therefore to present a combined approach amalgamating the Carreau-Yasuda model, heat transfer and magnetohydrodynamics with complex geometric features in realistic arterial hemodynamics with extensive visualization and interpretation, in order to generalize and extend previous studies. In previous studies these features have been considered separately and not simultaneously as in the current study.* The present simulations reveal some novel features of biomagnetic hemodynamics in bifurcated arterial transport featuring a saccular aneurysm which are envisaged to be of relevance in furnishing improved characterization of the rheological biomagnetic hemodynamics of realistic aneurysmic bifurcations in clinical assessment, diagnosis and magnetic-assisted treatment of cardiovascular disease.

KEYWORDS: *Arterial bifurcation, Saccular aneurysm, Non-Newtonian flow, Magneto-hemodynamics, Finite Element Method; skin friction; biomagnetic therapy.*

NOMENCLATURE

A^*_1, A	Constants	B_0	Magnetic field
J	Electric current density	Pr	Prandtl Number
Gr	Grashof Number	p	Pressure
g	Gravitational vector	n	Power-law index
M	Magnetohydrodynamic parameter		
Re	Reynolds number	T_w	Temperature at wall
A_1	Rivlin-Ericksen Tensor	V	Velocity vector
T_0	Reference temperature	u	Velocity in x-direction
C_f	Skin-friction coefficient	v	Velocity in y-direction
		Q	Volumetric flow rate
T	Temperature		

Greek Letters:

τ_s	Cauchy stress tensor	μ_∞	Infinite shear-rate viscosity
ρ	Density of the fluid	α	Womersley number
σ	Electrical conductivity	μ_0	Zero shear rate viscosity
μ	Fluid viscosity		
λ	Material time constant	$\dot{\gamma}$	Shear rate
θ	Non-dimensional temperature	k	Thermal conductivity of fluid

1. INTRODUCTION

Blood is an immensely complex aqueous ionic solution containing cellular elements and these elements include microscopic cells such as erythrocytes (red blood cells), leukocytes (white blood cells), thrombocytes, lymphocytes and lipoproteins suspended in a continuous saline plasma. It enables the sustained and efficient transportation of oxygen and CO_2, nutrients, hormones and metabolic wastes, among many other functions, throughout the body to maintain cell-level metabolism. Blood circulation is also critical in maintaining the necessary regulation of the pH, osmotic pressure and temperature of the whole body and protecting it from microbial and mechanical damage [1]. The plasma generally behaves as a Newtonian fluid [2], is composed of water (93%) and electrolytes, organic molecules, numerous proteins (3%), and waste products, whereas the whole blood (a suspension of cells and highly viscous in nature), exhibits the property of a non-Newtonian fluid, in particular in smaller vessels. At high shear rate blood usually behaves like a Newtonian fluid as observed in large arteries [3, 4]. Arterial blood flow is fundamental to the human circulatory system, and the presence of arterial stenosis (constriction) adversely influences the health of the cardiovascular system [5]. Blood flows to the body organs and body cells through a complex network of arteries, veins, and capillaries. The motion of blood is due to continuous pumping by the heart as deoxygenated blood is transported to the heart from all the body organs through veins and the heart pumps oxygenated blood to the whole body through the arteries. Over the past few decades, an impressive number of comprehensive theoretical and experimental investigations related to blood flow in arteries in the presence of a stenosis have been conducted with various methodologies [6]. Relevant examples include Criminale et al. [7], comes with the results that the accurate identification of blood hemodynamics is an essential step in characterizing flow regimes that would govern processes in physiology and pathology. Mathur and Jain [8], developed the mathematical model to study the blood flow behavior in stenosed artery and investigated the effects of stenosis on the blood flow analytically. Tripathi et al. [9], investigated the pulsatile blood flow behavior in stenosed artery with the suspension of hybrid nanofluid. The simulated results of the study shows the significant effect of hybrid nanofluid on the flow rate and wall shear stress. More recently *non-Newtonian hemodynamics* has been addressed by a number of investigators. Reddy *et al.* [10] studied blood flow by treating the blood as a polar (couple stress) fluid, showing that significant deviation in flow characteristics arise compared with the classical Newtonian model. Several investigators have also analysed theoretically and computationally the contribution of blood rheology to coronary artery disease and cerebral aneurysms. Agrawal *et al*. [11] studied the shear-thinning characteristics of blood with a Carreau–Yasuda Model, for coil embolization as a mildly invasive endovascular method for treatment of a cerebral aneurysm. The study leads to the observation that the blood rheology exerts a prominent role in the performance of the coil which is aimed at reducing fluid loading of the blood vessel and delaying subsequent vessel wall deformation.

Simulation of blood flow has been widely used in recent decades for better understanding the symptomatic spectrum of various diseases in order to improve already existing treatments, or to develop new therapeutic techniques. The characteristics of blood flow in an artery can be modified significantly by arterial disease, which may include aneurysms and stenoses. The domain of hemodynamics has grown into a significant branch of modern fluid mechanics and includes an extensive number of theoretical and experimental investigations. In the initial stages of arterial disease, arteriosclerotic lesions (stenoses) are not distributed randomly within the arterial network as they usually appear around junctions of arteries, arterial curvatures and bifurcations of large and medium arteries, where the usual flow patterns are significantly altered resulting in complexities in the cardiovascular system [12]. As a result of the complex flow phenomena owing to the continuous development of stenoses, it often becomes extremely difficult to distinguish these disturbances from the normal flow characteristics in these critical regions. Hence hemodynamical studies play an essential role in elucidating blood flow around bends and bifurcations in many large arteries as well as in various arterial diseases. The various models and methodologies adopted in these studies are as diverse as the geometric parameters and hydrodynamic conditions of arterial bifurcations. These have been comprehensively reviewed in by Lou and Yang [13] who emphasized that in low wall shear stress and recirculation regions such hemodynamic patterns play an important role in the development of atherosclerotic lesion and their subsequent progression. Furthermore, physiological risk factors such as hypertension, hyperlipidemia, high blood pressure and diabetes mellitus, are known to be major causes of atherosclerosis and aneurysms. Seo [14] and Zhang *et al.* [15] described numerical simulations of blood flow behavior in the bifurcated carotid artery. Seo [14] discussed the wall shear stress (WSS) distributions as well as pressure profiles due to the shear thinning behavior in both the internal carotid artery and external carotid artery and showed computationally that the variation of the flow characteristics can be dependent on the arterial bifurcation geometry which exerts an important role in the development of atherosclerosis. Zhang *et al.* [15] computed the wall shear stress and wall pressure gradient in the left as well as right coronary artery bifurcation identifying that the region of low wall shear stress (WSS) and magnitudes of maximum wall pressure gradient (WPG) increases with the angles of bifurcation. Further investigations also concluded that the initiation of the type of aneurysm is likely to be strongly influenced by the geometry of the arteries [16, 17]. The inner curved arterial walls and zones in the vicinity of flow separation at the bifurcation, are strongly associated with initial development of atherosclerosis and aneurysms. Therefore, the local flow patterns in curved locations and bifurcations are of significant relevance to the study of atherogenesis. In order to quantify accurately hydrodynamic characteristics in the regions of recirculation and separation at curved locations and bifurcations, numerous studies have been performed in recent years [18-20].

The role of hemodynamics in the growth of aneurysms has in particular stimulated considerable interest among researchers. Valencia *et al.*,[21] studied the effect of saccular (intercranial) aneurysms on blood flow in the artery with non-Newtonian and Newtonian fluid models. Rathish Kumar *et al*. [22] studied the blood flow in an asymmetrically dilated fusiform artery under pulsatile inflow conditions for a full cycle of period, *T*. Increasingly the Carreau-Yasuda bio rheological fluid model has attracted considerable attention from mathematicians and engineers due to its broad applications in quantifying non-Newtonian behavior of real blood. The Carreau-Yasuda fluid model has been implemented in blood flow computation by Khan *et al*. [22] for a diseased artery. Ali *et al.* [24] have investigated the biological interactions between Carreau fluid and micro-swimmers in undulating conduits (vessels) with a modified Taylor swimming sheet model, magnetic field and porous medium effects, motivated by microbot treatment of hemotological disorders.

"The presence of both ions in blood and iron in the haemoglobin molecule produces electrically conducting properties in blood. Streaming blood, can, therefore, be manipulated via the application of extracorporeal magnetic fields, which may be static or alternating. Arterial diseases such as arteriosclerosis and aneurysms, may, therefore, be treated via *biomagnetic therapy*. Magnetohydrodynamics (MHD) involves the motion of electrically conducting fluids under the influence of an applied magnetic field and arises in both Newtonian and non-Newtonian fluid flows. The emergence of new diverse technological applications of MHD, in medical engineering (magnetic blood separation, biomagnetics etc), chemical engineering, energy systems and materials processing, etc have stimulated high interest in magnetic fluid dynamic simulations in recent years. Extracorporeal magnetic field has a significant effect in reducing the flow velocity when needed which can be critical in flow regulation to mitigate disease. Gireesha *et al.* [25] studied the MHD fluid flow with the suspension of nanoparticles over a stretched sheet and investigated the influence of nanoparticle volume fraction and magnetic field on heat and mass transfer. Other studies have addressed the application of magnetic fields to manipulate nanoparticle concentration in fluid flow of relevance to nano-drug delivery [26-27]. Mahanthesh *et al.* [28], presented a detailed mathematical model for unsteady three-dimensional Eyring-Powell fluid flow under static magnetic field. They obtained extensive numerical results using a shooting technique coupled with a fourth-fifth order Runge–Kutta–Fehlberg scheme. Recently, Sreedevi *et al.*, [29,30], studied the effect of MHD heat and mass transfer on nanofluids containing single walled water-based carbon nanotubes (SWWNT) and multi-walled water-based carbon nanotubes in external flow from a vertical cone and internal flow between two stretchable rotating disks, respectively. They showed that with an increase in magnetic field parameter velocity is diminished and temperature is increased for both nanofluids. Reddy and Chamkha [31] considered the three-dimensional hydromagnetic flow of alumina-water nanofluid over a stretching sheet, observing that with an increment in magnetic field heat transfer is strongly modified. MHD blood flows also feature in electromagnetic medical pumps, where for some specific cardiac operations, magnetic fields can be used to regulate flow rates. In diseased arteries, the effect of *vessel tapering*, in addition to, the *shape* of stenosis also constitutes an exciting scenario for magnetic blood flow simulation. Nadeem *et al.* [32], discussed the effects of induced magnetic field on blood flow through stenosed vessels. This and other investigations have shown that the imposition of a magnetic field to streaming blood induces both electric and magnetic fields, which interact to generate a Lorentzian body force, which is resistive in nature and opposes the movement of blood [33, 34]. Vasu *et al.* [1], have more recently computed the MHD effect on blood flow through a stenosed coronary artery with extensive visualization, noting that blood velocity decreases with an increase in the magnetic field due to the Lorentz hydromagnetic drag force. Many different mathematical and computational studies have been reported on the influence of magnetization in arterial blood flow. Selvi and Ponalagusamy [35] investigated the effect of magnetic field on the two-phase oscillatory blood flow by assuming core and plasma regions as a Newtonian fluid in the arterial stenosis, showing that an increment in magnetic field elevates flow resistance of the blood flow in a stenosed artery. Ponalagusamy and Priyadharshini [36] extended the study in [35] to consider tapered stenotic and non-Newtonian effects in magnetized oscillatory two-phase blood flow. These studies however often neglected *heat transfer* effects which are also important since a key function of circulating blood is the transportation of heat. Prandtl numbers of streaming blood are known to be significantly higher than pure water and are critical to achieving thermo-regulatory functions in the cardiovascular system."

The theoretical and numerical studies dealing with the effects of heat transfer and magnetic field on the pulsatile flow of blood in a saccular aneurysm at the distant bifurcated aorta, with blood considered as a non-Newtonian fluid, have received comparatively less attention. Most studies are either experimental or three-dimensional computational simulation of aneurysm in the cerebral region neglecting rheological, biomagnetic and thermal effects. It has been observed that the blood flow velocity as well as wall shear stress decreases by exposing biological systems to an external magnetic field which permits a powerful mechanism for flow control in saccular aortic aneurysm treatment. Motivated by extending these studies to more realistic cases, the present article describes a detailed mathematical and numerical study of the *unsteady rheological magnetohydrodynamic blood flow, heat transfer in a bifurcated artery featuring a saccular aneurysm*. Also known as *berry* or inter-cranial aneurysms, they exhibit a characteristic rounded shape and are the most frequent contributor to non-traumatic subarachnoid hemorrhages. The Carreau-Yasuda [23, 24] model is utilized for non-Newtonian (hemo-rheological) characteristics. A Fourier heat conduction model is deployed for thermal conduction heat transfer and unsteady nonlinear coupled convective heat transfer is considered in streaming blood flow. With appropriate boundary conditions the normalized conservation equations are solved with the finite element method using a variational approach provided in the commercial software, FreeFem++ [1]. These aspects constitute the novelties of the present work. The results elaborate on the influence of several non-dimensional parameters (Reynolds number (Re) and Prandtl number (Pr)) and magnetic body force parameter on velocity, skin friction coefficient, temperature profile and volumetric flow rate at the aneurysmic section, in addition to throughout the remainder of the bifurcated artery domain. The simulations of the present study are envisaged to be of relevance in furnishing improved characterization of the biomagnetic hemodynamics of realistic aneurysm bifurcations which will be of benefit in more detailed assessment, diagnosis and magnetic-assisted treatment of cardiovascular diseases. This article has therefore been motivated by the growing clinical applications of non-intrusive magnetic-assisted techniques in 21st century treatments. The advantage of numerical blood flow simulation is that it provides almost limitless (and relatively inexpensive) insights which can aid decision-making processes during the treatment of cardiovascular diseases. Although a conventional method for treating the aneurysm is to deploy a stent or catheter inside the artery, however, nowadays targeting the drugs at desired locations is increasingly becoming the new standard. This also triggers the process of clotting formation at the diseased part and the effects of such post-treatment processes can also be predicted by computational simulation. Detailed interpretation of the computations is also provided of direct relevance to the magnetohydrodynamic treatment of rheological blood flow in diseased arterial systems. Additionally, the numerical simulations provide a useful compliment to clinical studies and may prove beneficial in testing the hypothesis of disease formation and furthermore may be of benefit in the design of cardiovascular devices, heart valves, stents, probes etc.

2. NON-NEWTONIAN THERMO-MAGNETIC BLOOD FLOW MODEL

An unsteady two-dimensional mathematical model for blood flow and coupled heat transfer in a bifurcated artery is considered wherein blood flow is modelled as non-homogeneous fluid. Blood rheology is simulated with the Carreau-Yasuda fluid model. Thermophysical properties are assumed constant. For the simulation, the pulsatile nature of blood has also been incorporated. The velocity is taken as zero at the walls of the vessel which is modelled as a bifurcated system with a singular saccular aneurysm. A Cartesian coordinate system (x, y, z) is adopted where flow in the z-direction has been neglected i. e. the flow is simulated only in the *x*-*y* plane as shown in **Fig. (1).**

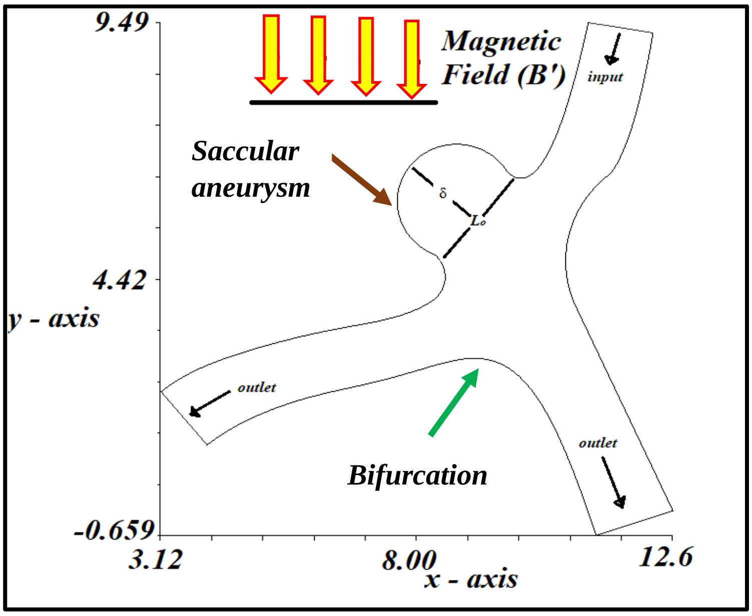

Figure 1. Schematic illustration of bifurcated artery with intercranial (saccular) aneurysm

The fluid is incompressible. The bifurcated artery has a finite length L and contains a saccular aneurysm at the bifurcation of maximum height δ and length L_0.

For unsteady flow of blood in the arterial vessel, the velocity vector V is assumed to be of the form:

$$V = [u, v, 0] \tag{1}$$

Here u and v are the velocity components in x *and* y directions. Blood is considered to be an incompressible Carreau-Yasuda non-Newtonian fluid, which is a complex viscosity rheological model originally developed for polymeric dynamics. Neglecting the body forces, the conservation equations for mass, momentum and energy (heat) for the blood transport may be presented in vectorial form as:

$$\nabla \cdot V = 0 \tag{2}$$

$$\rho\left(\frac{\partial V}{\partial t} + (V \cdot \nabla)V\right) = divT_s + J \times B' \tag{3}$$

$$\rho c_p\left(\frac{\partial T}{\partial t}+(V\cdot\nabla)T\right)=k\nabla^2 T \tag{4}$$

In equation (3) the second term on the right-hand side is the contribution due to applied magnetic field in electrically-conducting blood flow. Ohm's law provides a relation between *J* and *B'*:

$$J=\sigma(E+V\times B') \tag{5}$$

Here *E* represents the electric field, B' = B_0 + *b* represents the total magnetic field, σ is the electrical conductivity of blood, ***V*** is the velocity vector and ***J*** represents the electric current density. For small magnetic Reynolds number, the induced magnetic field is neglected. Hence:

$$J\times B'=-\sigma B_0^{\,2}V \tag{6}$$

Ignoring magnetic induction effects, the governing conservation equations for unsteady, incompressible two-dimensional rheological blood flow and heat transfer may be stated as follows by amalgamating the previous saccular geometric model of Valencia *et al.* [21] and Kumar *et al.* [22], heat transfer model of Khan and Hashim [23] and magnetohydrodynamic biological Carreau-Yasuda flow model of Ali *et al*. [24]:

$$\frac{\partial u}{\partial x}+\frac{\partial v}{\partial y}=0 \tag{7}$$

$$\rho\left(\frac{\partial u}{\partial t}+u\frac{\partial u}{\partial x}+v\frac{\partial u}{\partial y}\right)=-\frac{\partial p}{\partial x}+\frac{\partial}{\partial x}(S_{xx})+\frac{\partial}{\partial y}(S_{xy})+\sigma B_0^{\,2}u \tag{8}$$

$$\rho\left(\frac{\partial v}{\partial t}+u\frac{\partial v}{\partial x}+v\frac{\partial v}{\partial y}\right)=-\frac{\partial p}{\partial y}+\frac{\partial}{\partial x}(S_{xy})+\frac{\partial}{\partial y}(S_{yy}) \tag{9}$$

$$\rho c_p\left(\frac{\partial T}{\partial t}+u\frac{\partial T}{\partial x}+v\frac{\partial T}{\partial y}\right)=k\left(\frac{\partial^2 T}{\partial x^2}+\frac{\partial^2 T}{\partial y^2}\right) \tag{10}$$

The corresponding boundary conditions are:

$$\begin{array}{ll} u=0,\ v=0,\ T=T_w,\ p=p_1=A^*_1\cos^2(\omega t) & at\ wall \\ u=U_w=A\sin^2(\omega t),\ v=U_w=A\sin^2(\omega t), & at\ outlet \\ u=0,\ v=0,\ T=0 & at\ t=0\,(inlet) \end{array} \tag{11}$$

The constitutive equation for the Cauchy stress tensor in a Carreau-Yasuda fluid [23, 24] is given by

$$T_S=-pI+S \tag{12}$$

Here
$$S=\mu A_1 \tag{13}$$

With
$$\mu=[\mu_\infty+(\mu_0-\mu_\infty)[1+\lambda^2|\dot{\gamma}|^2]^{\frac{n-1}{2}}] \tag{14}$$

Here a more practical case has been considered, where in $\mu_0 >> \mu_\infty$. Hence μ_∞ is taken to be zero and consequently equation (14) reduces to:

$$\mu = [\mu_0 [1 + \lambda^2 |\dot{\gamma}|^2]^{\frac{n-1}{2}}] \tag{15}$$

Hence
$$S = [\mu_0 [1 + \lambda^2 |\dot{\gamma}|^2]^{\frac{n-1}{2}}] A_1 \tag{16}$$

In the above equations, μ_∞, μ_0 are infinite rate viscosity and zero rate viscosity of blood. In Eqn. (13), due to the restraint of incompressibility, $-pI$ represents the spherical stress, and the kinematical tensor A_1, can be defined by the following equations:

$$A_1 = \nabla V + (\nabla V)^t \tag{17}$$

$$\dot{\gamma} = \frac{1}{2} tr(A_1)^2$$

and

$$\dot{\gamma} = \left[4\left(\frac{\partial u}{\partial x}\right)^2 + \left(\frac{\partial u}{\partial y} + \frac{\partial v}{\partial x}\right)^2 \right]^{\frac{1}{2}} \tag{18}$$

Using the equations (16) and (18), the equations (7) - (10) become:

$$\frac{\partial u}{\partial x} + \frac{\partial v}{\partial y} = 0 \tag{19}$$

$$\begin{aligned} \rho\left[\frac{\partial u}{\partial t} + u\frac{\partial u}{\partial x} + v\frac{\partial u}{\partial y}\right] = -\frac{\partial p}{\partial x} + \left[\mu_0 \left\{1 + \lambda^2 \left|4\left(\frac{\partial u}{\partial x}\right)^2 + \left(\frac{\partial u}{\partial y} + \frac{\partial v}{\partial x}\right)^2\right|\right\}^{\frac{n-1}{2}}\right]\left(\frac{\partial^2 u}{\partial x^2} + \frac{\partial^2 u}{\partial y^2}\right) \\ +2\frac{\partial u}{\partial x}\frac{\partial}{\partial x}\left[\mu_0 \left\{1 + \lambda^2 \left|4\left(\frac{\partial u}{\partial x}\right)^2 + \left(\frac{\partial u}{\partial y} + \frac{\partial v}{\partial x}\right)^2\right|\right\}^{\frac{n-1}{2}}\right] \\ +\left(\frac{\partial u}{\partial y} + \frac{\partial v}{\partial x}\right)\frac{\partial}{\partial y}\left[\mu_0 \left\{1 + \lambda^2 \left|4\left(\frac{\partial u}{\partial x}\right)^2 + \left(\frac{\partial u}{\partial y} + \frac{\partial v}{\partial x}\right)^2\right|\right\}^{\frac{n-1}{2}}\right] + \sigma B_0^2 u \end{aligned} \tag{20}$$

$$\rho\left[\frac{\partial v}{\partial t}+u\frac{\partial v}{\partial x}+v\frac{\partial v}{\partial y}\right]=-\frac{\partial p}{\partial y}+\left[\mu_0\left\{1+\lambda^2\left|4\left(\frac{\partial u}{\partial x}\right)^2+\left(\frac{\partial u}{\partial y}+\frac{\partial v}{\partial x}\right)^2\right|\right\}^{\frac{n-1}{2}}\right]\left(\frac{\partial^2 v}{\partial x^2}+\frac{\partial^2 v}{\partial y^2}\right)$$
$$+2\frac{\partial v}{\partial x}\frac{\partial}{\partial y}\left[\mu_0\left\{1+\lambda^2\left|4\left(\frac{\partial u}{\partial x}\right)^2+\left(\frac{\partial u}{\partial y}+\frac{\partial v}{\partial x}\right)^2\right|\right\}^{\frac{n-1}{2}}\right] \quad (21)$$
$$+\left(\frac{\partial u}{\partial y}+\frac{\partial v}{\partial x}\right)\frac{\partial}{\partial x}\left[\mu_0\left\{1+\lambda^2\left|4\left(\frac{\partial u}{\partial x}\right)^2+\left(\frac{\partial u}{\partial y}+\frac{\partial v}{\partial x}\right)^2\right|\right\}^{\frac{n-1}{2}}\right]$$

$$\rho c_p\left(\frac{\partial T}{\partial t}+u\frac{\partial T}{\partial x}+v\frac{\partial T}{\partial y}\right)=k\left(\frac{\partial^2 T}{\partial x^2}+\frac{\partial^2 T}{\partial y^2}\right) \quad (22)$$

The hemodynamic wall shear stress is:

$$\tau_w=\mu_0\left(\frac{\partial u}{\partial y}\right)[1+\lambda^2|\dot{\gamma}|^2]^{\frac{n-1}{2}}\Big|_{y=0} \quad (23)$$

Skin-friction is:

$$C_f=\frac{2\tau_w}{\rho_f U_w{}^2} \quad (24)$$

Volumetric flow rate is defined as:

$$Q=\int_0^x u\,x\,dx \quad (25)$$

It is judicious to introduce the scaled variables to transform the mathematical model:

$$\bar{u}=\frac{u}{U_0},\ \bar{v}=\frac{v}{U_0},\ \bar{y}=\frac{y}{L_0},\ \bar{x}=\frac{x}{L_0},\bar{t}=\frac{U_0}{L_0}t,\mathrm{Re}=\frac{\rho U_0 L_0}{\mu_0},\bar{A}=\frac{A}{U_0}$$
$$\bar{\theta}=\frac{T-T_0}{T_w-T_0},\bar{p}=\frac{L_0 p}{U_0\mu_0},\bar{A}_1^*=\frac{L_0 A^*_1}{U_0\mu_0},\bar{\omega}=\frac{L_0}{U_0}\omega,\mathrm{Pr}=\frac{\mu_0 c_p}{k},M^2=\frac{\sigma_1 B_0{}^2 L_0{}^2}{\mu_0} \quad (26)$$

Here U_0, L_0, μ_0, T_0 *and* T_w denote the reference velocity, reference length of the aneurysm, zero-shear rate viscosity, reference fluid temperature, vessel wall temperature in the arterial tube model, respectively. Implementing Eqns. (26) in Eqns. (19)-(22) the following system of dimensionless conservation equations emerges:

$$\frac{\partial \overline{u}}{\partial \overline{x}}+\frac{\partial \overline{v}}{\partial \overline{y}}=0 \tag{27}$$

$$\begin{aligned}\mathrm{Re}\left[\frac{\partial \overline{u}}{\partial \overline{t}}+\overline{u}\frac{\partial \overline{u}}{\partial \overline{x}}+\overline{v}\frac{\partial \overline{u}}{\partial \overline{y}}\right]=&-\frac{\partial \overline{p}}{\partial \overline{x}}+\left[\left\{1+\lambda^2\left(\frac{U_0}{L_0}\right)^2\left|4\left(\frac{\partial \overline{u}}{\partial \overline{x}}\right)^2+\left(\frac{\partial \overline{u}}{\partial \overline{y}}+\frac{\partial \overline{v}}{\partial \overline{x}}\right)^2\right|\right\}^{\frac{n-1}{2}}\right]\left(\frac{\partial^2 \overline{u}}{\partial \overline{x}^2}+\frac{\partial^2 \overline{u}}{\partial \overline{y}^2}\right)\\&+2\frac{\partial \overline{u}}{\partial \overline{x}}\frac{\partial}{\partial \overline{x}}\left[\left\{1+\lambda^2\left(\frac{U_0}{L_0}\right)^2\left|4\left(\frac{\partial \overline{u}}{\partial \overline{x}}\right)^2+\left(\frac{\partial \overline{u}}{\partial \overline{y}}+\frac{\partial \overline{v}}{\partial \overline{x}}\right)^2\right|\right\}^{\frac{n-1}{2}}\right]\\&+\left(\frac{\partial \overline{u}}{\partial \overline{y}}+\frac{\partial \overline{v}}{\partial \overline{x}}\right)\frac{\partial}{\partial \overline{y}}\left[\left\{1+\lambda^2\left(\frac{U_0}{L_0}\right)^2\left|4\left(\frac{\partial \overline{u}}{\partial \overline{x}}\right)^2+\left(\frac{\partial \overline{u}}{\partial \overline{y}}+\frac{\partial \overline{v}}{\partial \overline{x}}\right)^2\right|\right\}^{\frac{n-1}{2}}\right]+M^2\overline{u}\end{aligned} \tag{28}$$

$$\begin{aligned}\mathrm{Re}\left[\frac{\partial \overline{v}}{\partial \overline{t}}+\overline{u}\frac{\partial \overline{v}}{\partial \overline{x}}+\overline{v}\frac{\partial \overline{v}}{\partial \overline{y}}\right]=&-\frac{\partial \overline{p}}{\partial \overline{y}}+\left[\left\{1+\lambda^2\left(\frac{U_0}{L_0}\right)^2\left|4\left(\frac{\partial \overline{u}}{\partial \overline{x}}\right)^2+\left(\frac{\partial \overline{u}}{\partial \overline{y}}+\frac{\partial \overline{v}}{\partial \overline{x}}\right)^2\right|\right\}^{\frac{n-1}{2}}\right]\left(\frac{\partial^2 \overline{v}}{\partial \overline{x}^2}+\frac{\partial^2 \overline{v}}{\partial \overline{y}^2}\right)\\&+2\frac{\partial \overline{v}}{\partial \overline{y}}\frac{\partial}{\partial \overline{y}}\left[\left\{1+\lambda^2\left(\frac{U_0}{L_0}\right)^2\left|4\left(\frac{\partial \overline{u}}{\partial \overline{x}}\right)^2+\left(\frac{\partial \overline{u}}{\partial \overline{y}}+\frac{\partial \overline{v}}{\partial \overline{x}}\right)^2\right|\right\}^{\frac{n-1}{2}}\right]\\&+\left(\frac{\partial \overline{u}}{\partial \overline{y}}+\frac{\partial \overline{v}}{\partial \overline{x}}\right)\frac{\partial}{\partial \overline{x}}\left[\left\{1+\lambda^2\left(\frac{U_0}{L_0}\right)^2\left|4\left(\frac{\partial \overline{u}}{\partial \overline{x}}\right)^2+\left(\frac{\partial \overline{u}}{\partial \overline{y}}+\frac{\partial \overline{v}}{\partial \overline{x}}\right)^2\right|\right\}^{\frac{n-1}{2}}\right]\end{aligned} \tag{29}$$

$$\mathrm{Re}\,\mathrm{Pr}\left(\frac{\partial \overline{\theta}}{\partial \overline{t}}+\overline{u}\frac{\partial \overline{\theta}}{\partial \overline{x}}+\overline{v}\frac{\partial \overline{\theta}}{\partial \overline{y}}\right)=\left(\frac{\partial^2 \overline{\theta}}{\partial \overline{x}^2}+\frac{\partial^2 \overline{\theta}}{\partial \overline{y}^2}\right) \tag{30}$$

Consequently, with boundary-layer approximations, the above equations emerge in non-dimensional form as:

$$\frac{\partial \overline{u}}{\partial \overline{x}}+\frac{\partial \overline{v}}{\partial \overline{y}}=0 \tag{31}$$

$$\mathrm{Re}\left[\frac{\partial \bar{u}}{\partial \bar{t}}+\bar{u}\frac{\partial \bar{u}}{\partial \bar{x}}+\bar{v}\frac{\partial \bar{u}}{\partial \bar{y}}\right]=-\frac{\partial \bar{p}}{\partial \bar{x}}+\left[\left\{1+\lambda^{2}\left(\frac{U_0}{L_0}\right)^{2}\left|\left(\frac{\partial \bar{u}}{\partial \bar{y}}\right)^{2}\right|\right\}^{\frac{n-1}{2}}\right]\left(\frac{\partial^{2} \bar{u}}{\partial \bar{y}^{2}}\right)$$
$$+\left(\frac{\partial \bar{u}}{\partial \bar{y}}\right)\frac{\partial}{\partial \bar{y}}\left[\left\{1+\lambda^{2}\left(\frac{U_0}{L_0}\right)^{2}\left|\left(\frac{\partial \bar{u}}{\partial \bar{y}}\right)^{2}\right|\right\}^{\frac{n-1}{2}}\right] \qquad (32)$$
$$+M^{2}\bar{u}$$

$$\frac{\partial \bar{v}}{\partial \bar{t}}+\frac{\partial \bar{p}}{\partial \bar{y}}=0 \qquad (33)$$

$$\mathrm{Re}\,\mathrm{Pr}\left(\frac{\partial \bar{\theta}}{\partial \bar{t}}+\bar{u}\frac{\partial \bar{\theta}}{\partial \bar{x}}+\bar{v}\frac{\partial \bar{\theta}}{\partial \bar{y}}\right)=\left(\frac{\partial^{2} \bar{\theta}}{\partial \bar{x}^{2}}+\frac{\partial^{2} \bar{\theta}}{\partial \bar{y}^{2}}\right) \qquad (34)$$

The associated non-dimensional boundary conditions now take the form:

$$\begin{aligned}
&\bar{u}=0,\ \bar{v}=0,\ \bar{\theta}=1,\ \bar{p}=\bar{A}_1^{*}\cos^{2}(\bar{\omega}\bar{t}) && \text{at wall}\\
&\bar{u}=\bar{A}\sin^{2}(\bar{\omega}\bar{t}),\ \bar{v}=\bar{A}\sin^{2}(\bar{\omega}\bar{t}), && \text{at outlet} \qquad (35)\\
&\bar{u}=0,\ \bar{v}=0,\ \bar{\theta}=0 && \text{at } \bar{t}=0\,(\text{inlet})
\end{aligned}$$

3. FINITE ELEMENT SIMULATION WITH FreeFEM++

The non-dimensional magnetic bio-rheological blood flow boundary value problem defined by Eqns. (31)-(34) with boundary conditions (35) is formidable owing to strong nonlinearity, the coupling of many different variables, inclusion of two space variables and time. A robust computational scheme is, therefore, essential to obtain fast and rapidly convergent solutions. Finite element has been used vastly over different physical problems. The finite element method involves dividing the domain of the problem into a collection of subdomains, with each subdomain represented by a set of element equations to the original problem, followed by systematically recombining all sets of element equations into a global system of equations for the final calculation. FEM's popularity has been increasing due to the greater flexibility it offers in modeling complex geometries. FEM has a solid theoretical foundation which gives added reliability and makes it possible to mathematically analyse and estimate the error in the approximate solution. Many researchers have employed finite element methods for engineering simulations. Reddy et al. [37], investigated the carbon nanotube nanofluid flow and heat transfer with thermal radiation flux between two stretchable rotating disks using finite element method. Reddy et al. [38], employed a variational finite element method to simulate the nanofluid flow over a vertical cone. Sreedevi et al. [39] computed the heat and mass transfer for Al_2O_3 and TiO_2 nanofluids over a wedge and with a Galerkin finite element method.

Many studies of medical fluid dynamics have been reported using finite element techniques. Rajashekhar *et al.* [40] investigated two-dimensional steady blood flow through an arterial bifurcation by employing finite element analysis (FEA) with different geometries. Rehman et al. [41], employed finite element method to study the heat transfer due to heated elliptical cylinder in a rectangular chamber having heated triangular ribs. They have also considered triangular finite elements for the meshing of the domain with/without heated triangular ribs. Very recently Rehman *et al.* [42-44], employed the finite element method to study the heat transfer in different shaped domains such as hexagonal, rhombus and trapezium geometries with T-shaped flipper and hybrid meshes i.e., both triangular and rectangular shaped elements. The concept of hybrid meshing has also been employed by Zahri *et al.* [45] in magnetized rectangular chamber optimization (TMRCO).

In the present study the finite element method (FEM) [46], with the variational approach, as available in the FreeFEM++ software, has been used wherein time discretization is achieved with a Crank-Nicolson scheme. To obtain a weak formulation of the system of differential Eqns. (31-34) the function spaces have been defined as:

$$
\begin{aligned}
X &= \left\{ \overline{u} \in \left(H_1(\Omega) \right) \middle| \overline{u} = a \ on \ \Gamma_{in}, \overline{u} = 0 \ on \ \Gamma_{wall} \right\} \\
Q &= \left\{ \overline{u} \in \left(H_1(\Omega) \right) \middle| \overline{u} = 0 \ on \ \Gamma_{in} \cup \Gamma_{wall} \right\}
\end{aligned}
\tag{36}
$$

The *weak form* of Eqns. (31) - (34) is obtained by determining w ∈ X and ϕ, θ ∈ P such that every $v \in Q$ and $q \in P$ where $P = L^2(\Omega)$. A fundamental aspect of the current modeling is to obtain a *robust weak form* of the above system of Eqns. (31)-(34). To achieve *smoothness of the solution* which is bounded due to the weaker restriction, these differential equations cannot be solved directly. Therefore, the finite dimensional subspaces have to be defined as $Q_h \subset Q$ and $P_h \subset P$. Let us consider the finite dimensional approximations as $u_h, v_h, w_h \subset Q_h$ and $q_h \subset P_h$. In view of the finite dimensional approximation, the set of Eqns. (31)-(34) becomes:

$$
\int_{\Omega} \frac{\partial \overline{u}}{\partial \overline{x}} \cdot u_h d\Omega + \int_{\Omega} \frac{\partial \overline{v}}{\partial \overline{y}} \cdot u_h d\Omega = 0 \tag{37}
$$

$$\int_{\Omega} \mathrm{Re}\frac{\partial \bar{u}}{\partial \bar{t}} \cdot v_h d\Omega + \int_{\Omega} \mathrm{Re}\,\bar{u}\frac{\partial \bar{u}}{\partial \bar{x}} \cdot v_h d\Omega + \int_{\Omega} \mathrm{Re}\,\bar{v}\frac{\partial \bar{u}}{\partial \bar{y}} \cdot v_h d\Omega = -\int_{\Omega} \frac{\partial \bar{p}}{\partial \bar{x}} \cdot v_h d\Omega$$
$$+\int_{\Omega} \left(\frac{\partial^2 \bar{u}}{\partial \bar{y}^2}\right)\left[\left\{1+\lambda^2\left(\frac{U_0}{L_0}\right)^2\left|\left(\frac{\partial \bar{u}}{\partial \bar{y}}\right)^2\right|\right\}^{\frac{n-1}{2}}\right] \cdot v_h d\Omega$$
$$+\int_{\Omega} (n-1)\lambda^2\left(\frac{\partial \bar{u}}{\partial \bar{y}}\right)^2\frac{\partial^2 \bar{u}}{\partial \bar{y}^2}\left[\left\{1+\lambda^2\left(\frac{U_0}{L_0}\right)^2\left|\left(\frac{\partial \bar{u}}{\partial \bar{y}}\right)^2\right|\right\}^{\frac{n-3}{2}}\right] \cdot v_h d\Omega$$
$$+\int_{\Omega} M^2\bar{u} \cdot v_h d\Omega \tag{38}$$

$$\int_{\Omega} \frac{\partial \bar{v}}{\partial \bar{t}} \cdot w_h d\Omega + \int_{\Omega} \frac{\partial \bar{p}}{\partial \bar{y}} \cdot w_h d\Omega = 0 \tag{39}$$

$$\int_{\Omega} \mathrm{Re}\,\mathrm{Pr}\frac{\partial \bar{\theta}}{\partial \bar{t}} \cdot q_h d\Omega + \int_{\Omega} \mathrm{Re}\,\mathrm{Pr}\,\bar{u}\frac{\partial \bar{\theta}}{\partial \bar{x}} \cdot q_h d\Omega + \int_{\Omega} \mathrm{Re}\,\mathrm{Pr}\,\bar{v}\frac{\partial \bar{\theta}}{\partial \bar{y}} \cdot q_h d\Omega = \int_{\Omega} \left(\frac{\partial^2 \bar{\theta}}{\partial \bar{x}^2} + \frac{\partial^2 \bar{\theta}}{\partial \bar{y}^2}\right) \cdot q_h d\Omega \tag{40}$$

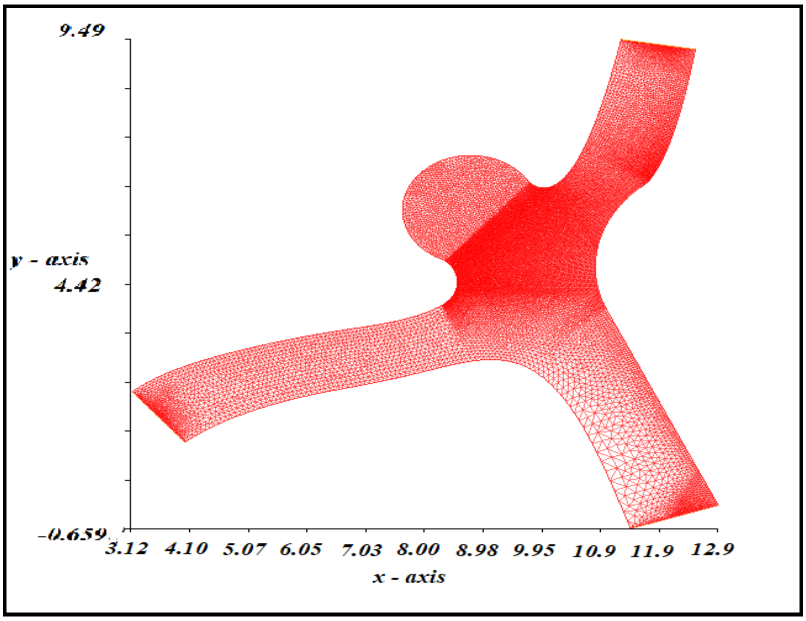

Figure 2. Unstructured fixed mesh of triangular elements

Eqns. (37)-(40) with boundary conditions (35) are solved numerically using the variational finite element method in FreeFEM++. In the present study we consider 6-node triangular elements (P_2) and design an appropriate finite element mesh (grid) comprising 48021 triangular elements and 145013 nodes, as presented above in **Figure 2**. In the fixed mesh the prescribed minimum step size ($h_{\min}$) is 0.013442 for all simulations.

4. MESH INDEPENDENCE ANALYSIS

By conducting several different finite element mesh (grid) distribution tests, it may be established whether the calculated numerical results are grid-independent or not. The numerical values for skin-friction coefficients, *at the aneurysm*, for various designs comprising unstructured fixed mesh elements with vertices and triangular elements, are provided in **Figure 3**. Twelve different mesh distributions have been tested to ensure the simulated numerical results are mesh independent. Therefore, the final optimized selected mesh for the present FREEFEM++ simulations consisted of **48021** triangular elements and **145013** nodes, respectively. From Table 1 and figure 3, it is evident that increasing the mesh element density beyond this design does not modify the numerical values for non-dimensional skin-friction coefficient significantly in the domain with the parametric values prescribed i. e. *Pr = 14, Re = 21 and M=0.6 (viscous force exceeds magnetic drag force)*. Physically this data is consistent with actual thermal blood properties under laminar flow with weak external magnetic field. Mesh independent results are therefore ensured with the mesh design comprising **145013** nodes and **48021** triangular elements (simulation number 11 in **Table 1**).

Table 1 (a). Grid Independency analysis with ***Pr = 14, Re = 21 and M=0.6.***

Simulation Number	Number of Elements	Number of Nodes	Skin-friction coefficient (Aneurysm)
1.	7908	12098	0.001857
2.	9044	13812	0.002393
3.	9882	30127	0.003558
4.	13634	41473	0.003636
5.	19672	59677	0.003785
6.	27407	83081	0.004003
7.	27466	83229	0.004881
8.	31068	94015	0.005873
9.	32931	99693	0.00592
10.	35949	108697	0.00626
11.	**48021**	**145013**	**0.006369**
12.	55335	167015	0.006668

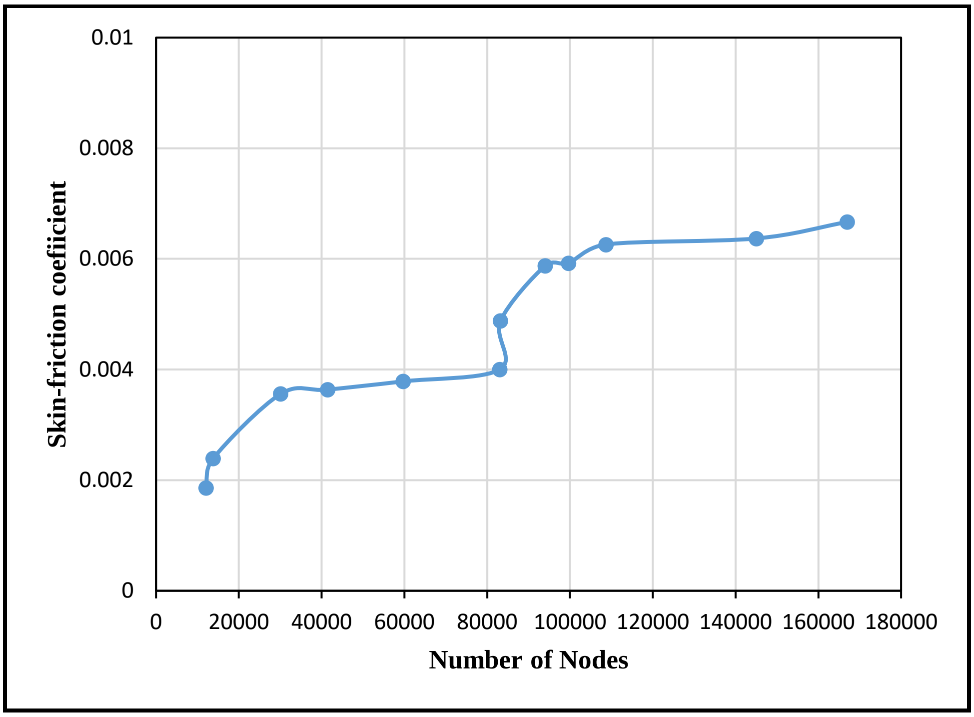

Figure 3 (a): Grid Independence study (skin-friction coefficient)

Table 3: Comparison of velocity (w) values, using the present scheme with the existing schemed results for fixed values of $\alpha = 5.0, \frac{\partial p}{\partial z} = 2, \sigma = 0.5, R(z) = 1, and\ R_2(z) = 0$ in the parent artery of arterial bifurcation.

r - axis	***Numerical value of velocity (w) given by Srinivasacharya et al. [47]***	***Value of velocity (w) by implementation of FEM on Srinivasacharya et al. [47] modelled problem***
0.00	0.00	0.00
0.1	0.00768	0.0070204
0.2	0.01398	0.013904
0.3	0.01856	0.018538
0.4	0.02118	0.020763
0.5	0.02179	0.021698
0.6	0.02049	0.020071
0.7	0.01740	0.017453
0.8	0.01274	0.012857
0.9	0.00679	0.006872
1.0	0.00	0.00

To validate the FREEFEM++ code which has been adopted to simulate the problem, benchmarking is conducted against the published results obtained by Srinivasacharya et al. [47] for velocity of viscous blood flow are compared with the results obtained by using FEM for the model and the comparisons are displayed in **Table 3**. From the table 3 it can be observed that the results acquired by using the method (FDM) and the FEM (variational approach) are match up to three decimal points. Hence it can be deduced that the achieved results testifying to the accuracy of the FREEFEM++ code. Also **figure 3(b) and 3(c)**, evidently close correlation of fluid behavior while comparing the Newtonian and Non-Newtonian fluid model (Carreau- Yasuda model) is achieved testifying to the accuracy of the FREEFEM++ code. Non-Newtonian fluid achieves higher velocity magnitudes than Newtonian fluids at intermediate times, but the reverse effect is computed at small times and high time values.

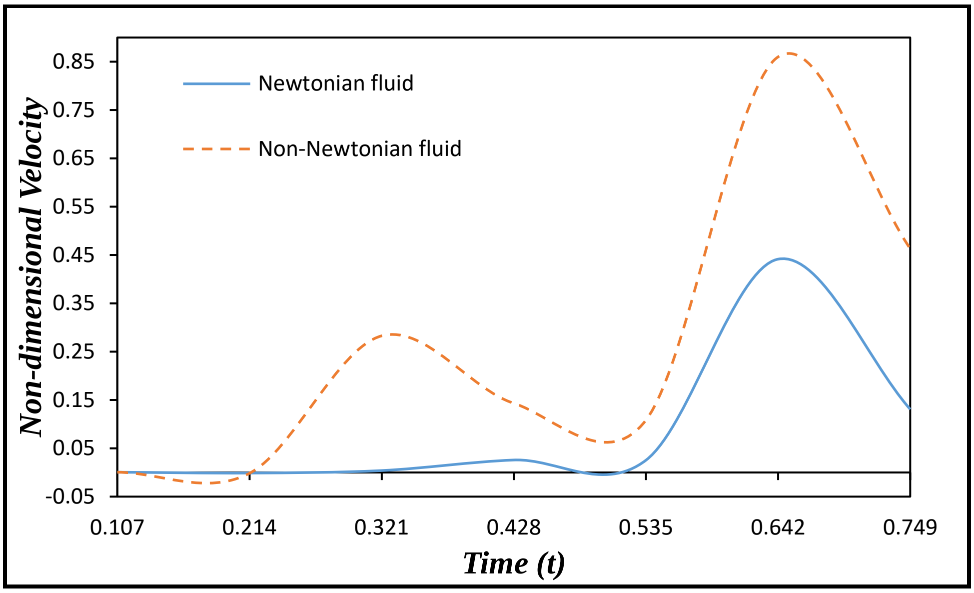

Figure 3 (b): Comparison of dimensionless velocity (u) values, with FREEFEM++ for Newtonian and non-Newtonian fluid at $x = 8.78, y = 7.00, M = 0.6, \mathrm{Re} = 521, \mathrm{Pr} = 14$.

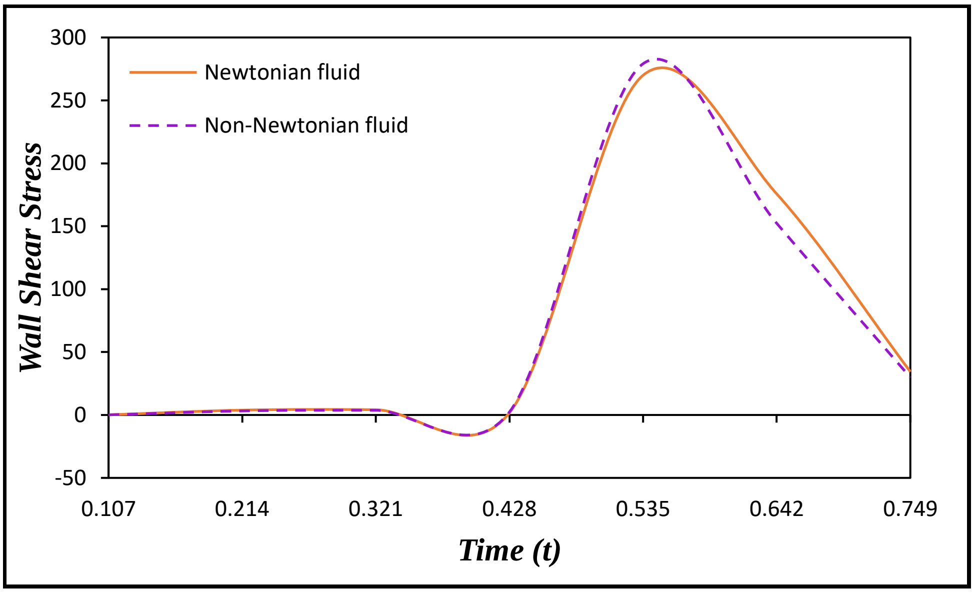

Figure 3 (c): Comparison of dimensionless wall shear stress values, with FREEFEM++ for Newtonian and non-Newtonian fluid at $x = 8.78, y = 7.00, M = 0.6, \mathrm{Re} = 521, \mathrm{Pr} = 14$.

5. FREEFEM++ RESULTS AND DISCUSSION

In this section, the quantitative effect of selected parameters i.e., magnetohydrodynamic body force parameter (*M*), Reynolds number (*Re*), and Prandtl number (*Pr*), on the velocity, temperature, pressure and skin-friction coefficient distributions with the variation of time are examined in detail. The results are all visualized via tables, contour plots, and graphs. In the computations, the default values of various parameters are as documented in **Table 2**.

Table 2: Prescribed parameter values implemented in FREEFEM++ computations.

Parameter	n	λ	δ	*Pr*	L	Re	ρ_f	*M*
Values	1.4	0.7	0.310	21	4.0	14	1060	0.6

Figures 4(a) – 4(d) depict the non-dimensional pressure contours for different values of Reynolds number for the *whole bifurcated arterial section* for fixed values of Prandtl number (*Pr*), MHD parameter (*M*) and time (*t*). The pressure initially decreases with the increment of Reynolds number (*Re*) at the saccular aneurysm as well as near its throat. As one can observe from the coloured contours present in the figure 4, the pressure increases while moving from the inlet arterial location to near the aneurysm wall and attains a *maximum near throat of the aneurysm;* thereafter pressure decreases to both outlets of the artery as the blood vessel widens which re-distributes the flow pressure. At higher Reynolds numbers, vortex and inertial effects are intensified. Hence, as can be seen from Figure 4, the wall pressure for *Re = 200* is reduced along the aneurytic region due to the flow separation formed close to the outer wall surface.

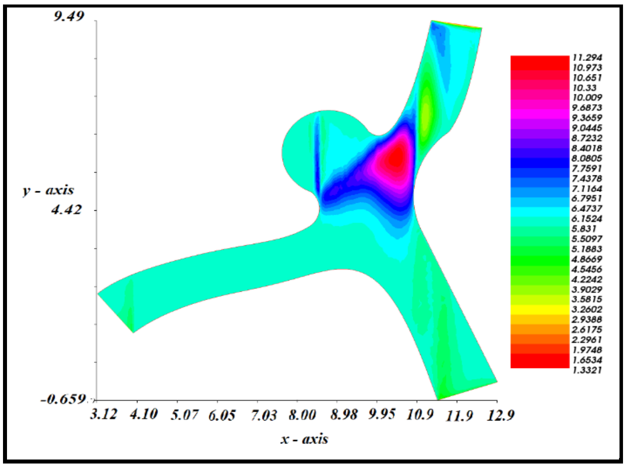

4(a)

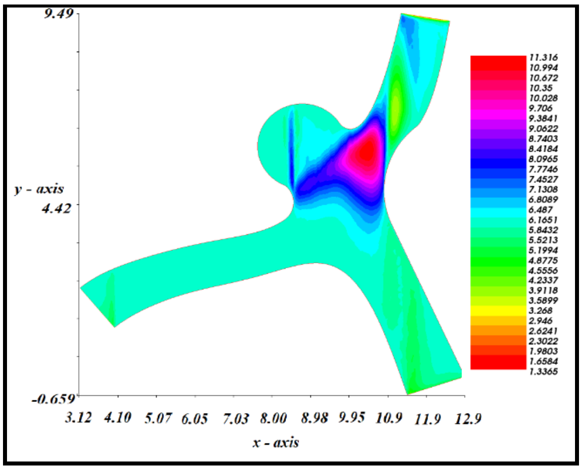

4(b)

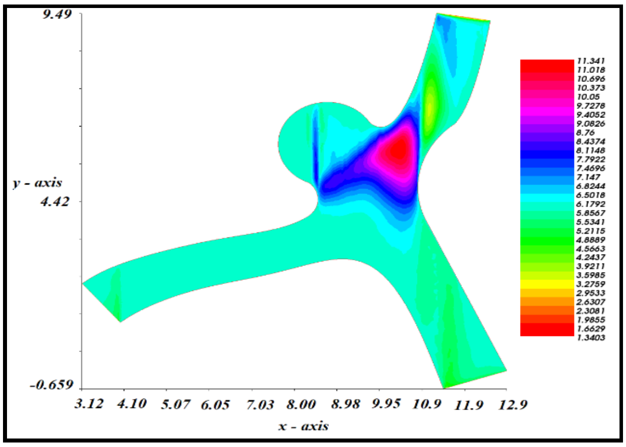

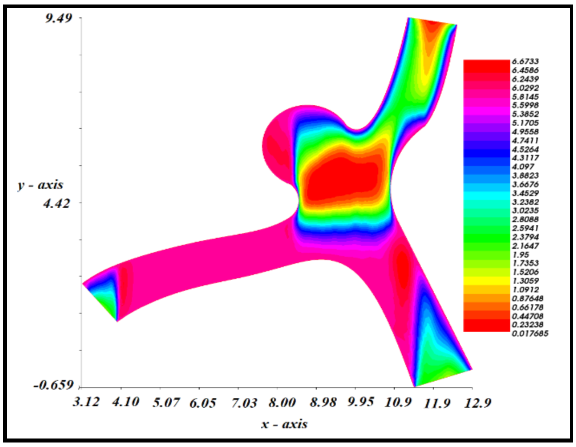

4(c) **4(d)**

Figure 4 Pressure distribution (a) $M = 0.6, Re = 14, Pr = 21\ and\ t = 0.4$ (b) $M = 0.6, Re = 21, Pr = 21\ and\ t = 0.4$ (c) $M = 0.6, Re = 100, Pr = 21\ and\ t = 0.4$ and (d) $M = 0.6, Re = 200, Pr = 21 and t = 0.4$

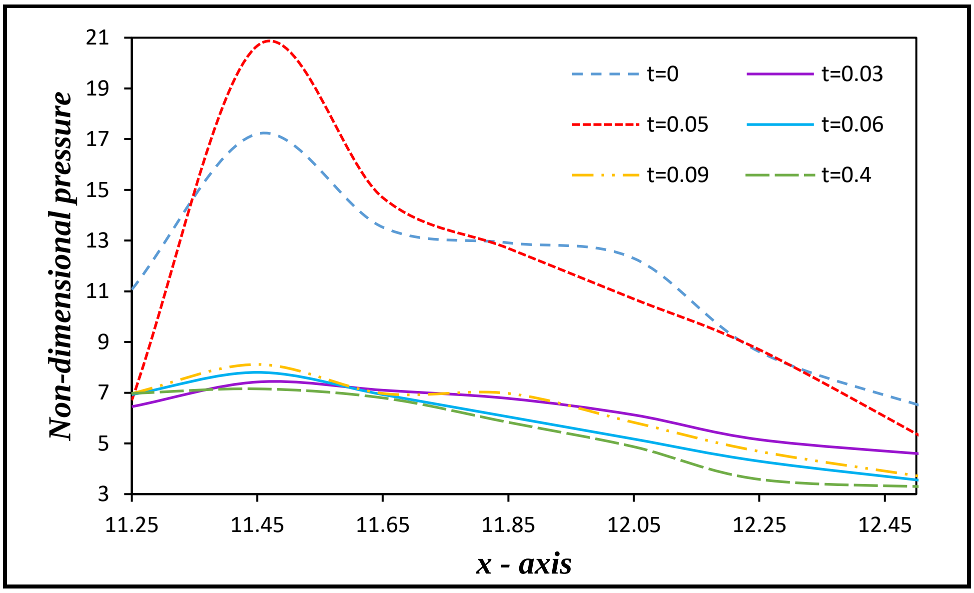

Figure 6 Effect of time (t) on pressure distribution in saccular aneurysm region for $Re = 14, Pr = 14, M = 0.6$, and $y = 9.08$.

Figure 6 shows the pressure distribution near the throat of the aneurysm (bulge) over a period of time with respect to axial axis and evidently pressure decreases as time increases. This is attributable to the widening of the arterial region *downstream* of the aneurysm which results in a relaxation in the distribution of pressure in both outlet arterial branches. **Figure 7** visualizes the pressure distribution near the throat of the saccular aneurysm over a time period but with respect to the *transverse* (y-) axis. As with the figure 6, the trend in figure 7 indicates a similar depletion in pressure decreases with time increment.

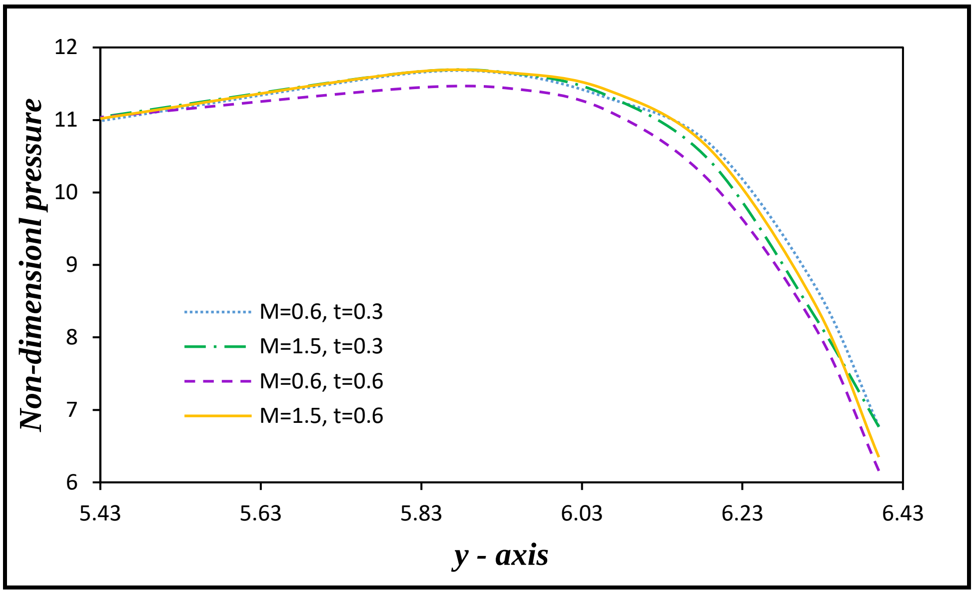

Figure 7 Effect of MHD parameter (*M*) on pressure distribution over different periods of time (*t*) in saccular aneurysm region for $Re = 21, Pr = 14, and x = 10.00$.

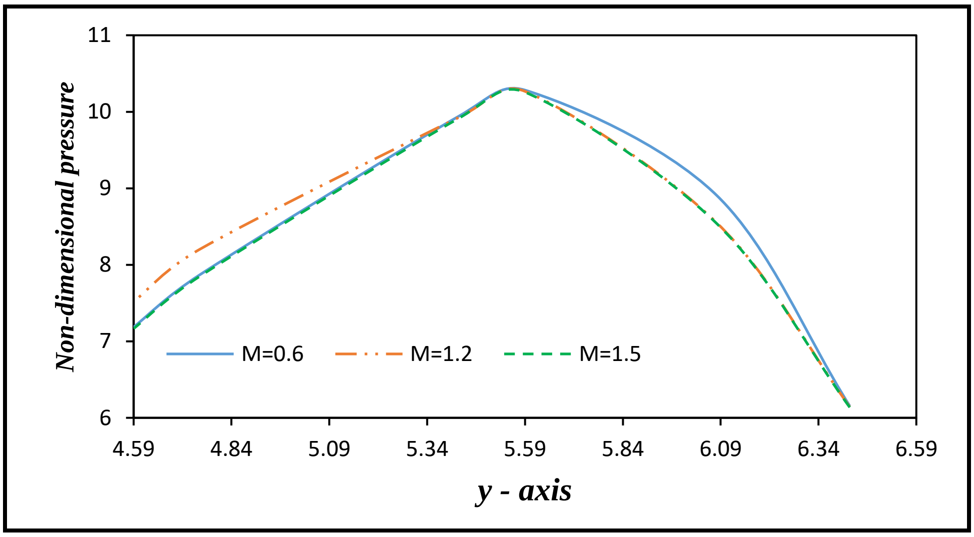

Figure 8 Effect of MHD parameter (*M*) on pressure distribution in saccular aneurysm region for $Re = 100, Pr = 14, t = 0.4$ and $x = 9.95$.

In figure 7 and 8, the pressure distribution in the vicinity of the throat of the aneurysm for two different Reynolds numbers i. e. 21 and 100 is computed. Clearly pressure also increases with increase in MHD parameter (*M*). This is attributable to the decelerating nature of Lorentzian magnetic drag which reduces velocities and results in a concomitant elevation in pressure (there is an inverse relationship between pressure and velocity). All the curves in both figures exhibit a gradual decay from their respective maximum value while moving towards the outer wall of the artery. It can be observed that with increasing magnetic field intensity, there is a significant variation in pressure for low Reynolds number (*Re = 21*) flow.

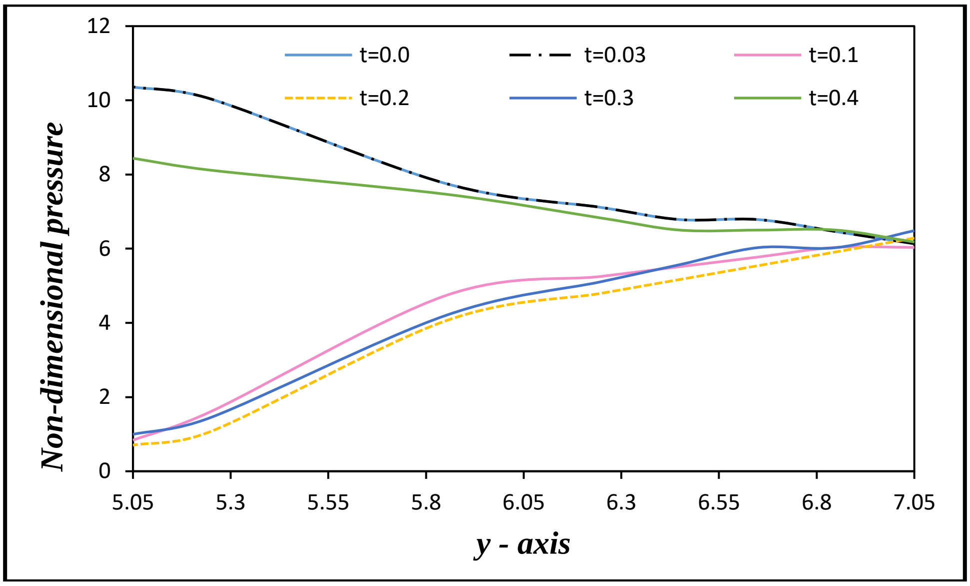

Figure 9 Effect of periodic time (t) over pressure distribution in saccular aneurysm region for $Re = 100, Pr = 14, M = 0.6$ *and* $x = 8.88$.

This variation is suppressed as the Reynolds number increases to 100, since the greater inertial force in the hemodynamic regime counteracts the impeding nature of the magnetic (Lorentzian) drag force. A similar observation for pressure distribution over an arterial segment with increment of Reynolds number and magnetic number has been earlier noted in [48]. The increment in Reynolds number, while remaining in the laminar regime, still greatly elevates the inertial force effect which accelerates the flow against the action of the magnetic field in the core flow and also at the vessel walls. This leads to a simultaneous decrement in pressure to the outer wall.

The non-dimensional pressure distribution for higher Reynolds number (*Re = 100*) *at the aneurysm* over various time periods has been described in **figure 9**. The pressure also decreases with respect to time and additionally decreases *towards the outer wall* of the aneurysm. The present unsteady simulations therefore hold the advantage that unlike most steady-state hemodynamic bifurcation aneurysm computations in the literature, time evolution in flow characteristics cannot be captured, which is of great relevance to actual behavior in clinical scenarios.

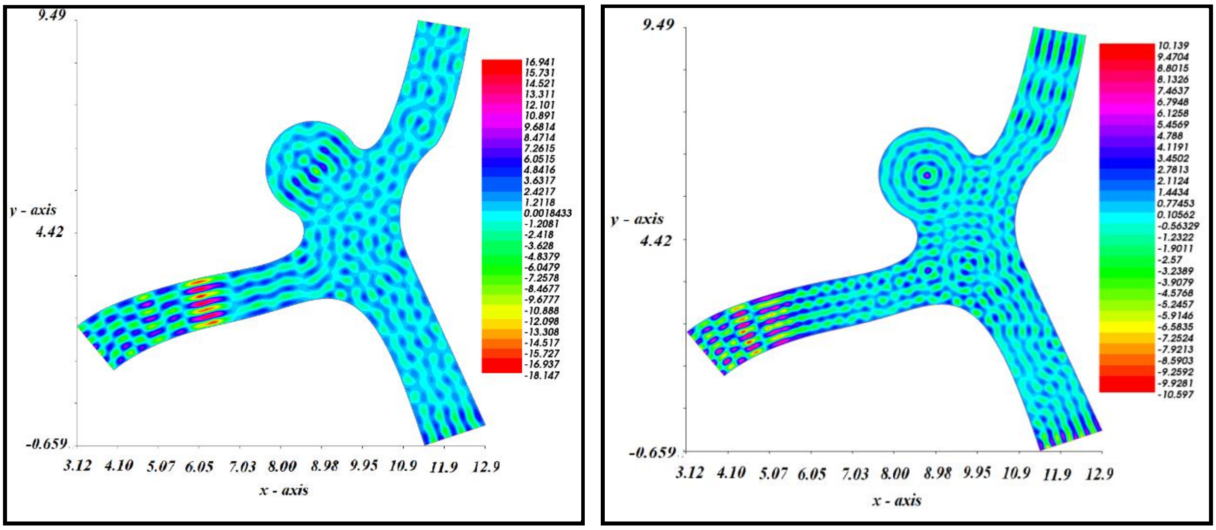

10(a) **10(b)**

Figure 10 Temperature distribution (a) $M = 1.2, \mathrm{Re} = 21$ *and* $\mathrm{Pr} = 14$ (b) $M = 1.2, \mathrm{Re} = 21$ *and* $\mathrm{Pr} = 21$.

Figure 10 (a) to 10 (b) depict the temperature contour distributions in the bifurcated arterial section. These coloured contours shows that the temperature *decreases* with increase of Prandtl number. For real blood flows, Victor and Shah [49] have shown that Prandtl numbers fall in the region 15 to 25. Since the Prandtl number is the ratio of momentum diffusivity to the thermal diffusivity hence larger values of Prandtl number represents the case of less heat transfer from the boundary to the fluid. The Prandtl number is also the product of dynamic viscosity and specific heat capacity divided by the thermal conductivity of the fluid. Therefore, increment in Prandtl number indicates decrement in thermal diffusivity. Heat diffuses slower in blood compared to, for example water or air, and this manifests in a temperature decrement, for Pr = 21 compared with Pr $=14$. This has important implications in homeostasis and the prescription of correct thermophysical data for the heat conducting characteristics of blood (often ignored in numerical models), provides a more realistic estimation of actual thermal characteristics.

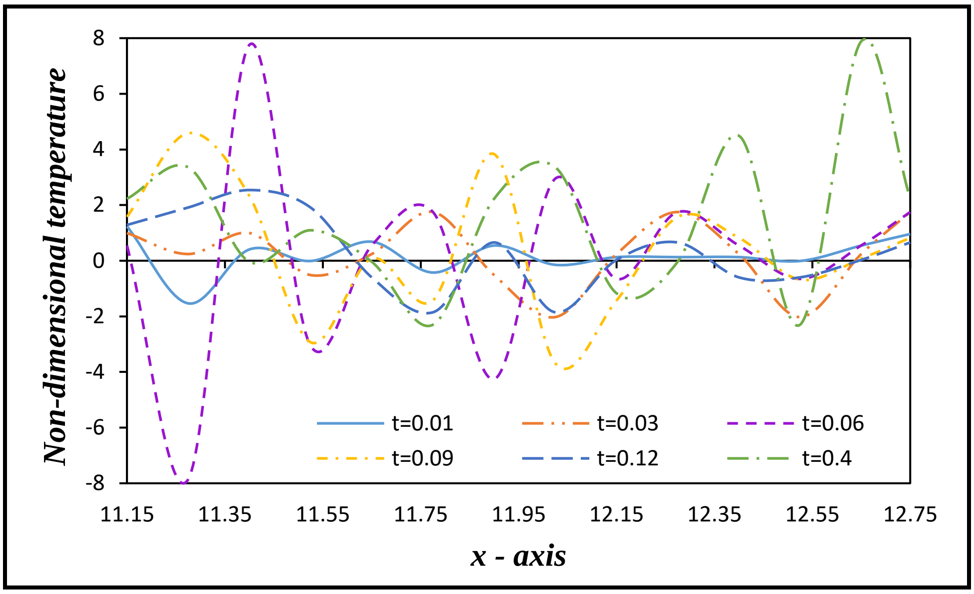

Figure 11 The temperature distribution over different time periods near the distal outlet of the bifurcated arterial region for $Re = 14, Pr = 14, y = 0.00 \; and \; M = 1.5$

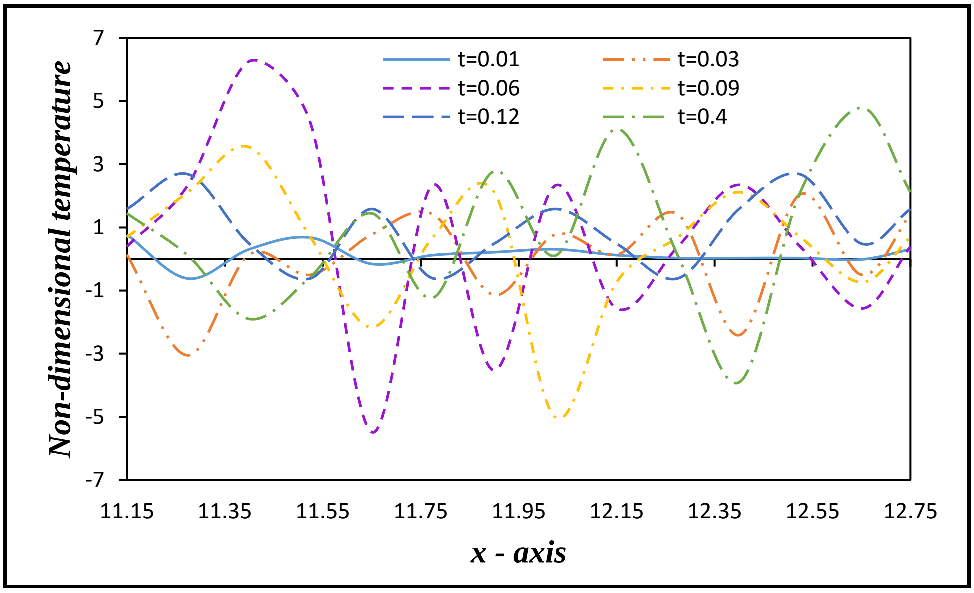

Figure 12 The temperature distribution over different time periods near the distal outlet of the bifurcated arterial region for $Re = 14, Pr = 21, y = 0.00 \; and \; M = 1.5$.

Figures 11 and 12, show the periodical variation in temperature at the distal outlet of the artery for different values of Prandtl number. The following graphs shows clearly that temperature increases with the *time increment* but decreases with elevation in Prandtl number from (*Pr* = 14 to *Pr* = 21) as increment in the Prandtl number causes decrement in thermal diffusivity and temperature decreases. Evidently therefore the thermal diffusion in streaming blood is assisted with progress in time which is an important factor linked to the time taken for the human being to acclimatize and absorb heat into the circulatory system, often as a by-product of food consumption. This effect is *not instantaneous* and takes time, as noted by Çinar *et al*. [50].

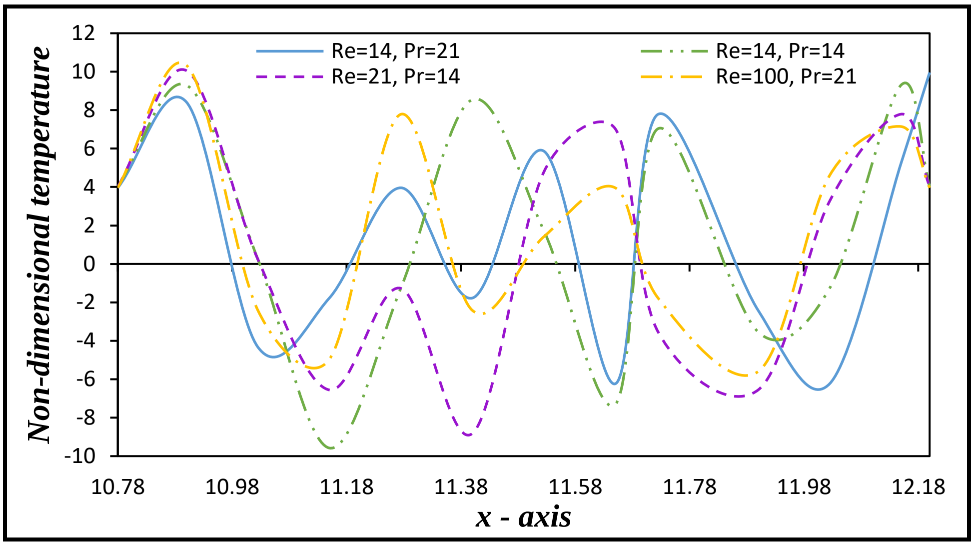

Figure 13 The temperature distribution for different values of Re and Pr near inlet of the bifurcated arterial region for $M = 0.6, t = 0.03, and\ y = 7.80$.

Figure 13 shows the temperature distribution over various values of Reynolds number (*Re = 14, 21 and 100*) and Prandtl number (*Pr =14, 21*) near the inlet of the artery. The graph shows that temperature *increases with an increment in Reynolds number* but decreases with an increment in Prandtl number. Again, the elevation in inertial force) Reynolds number expresses the ratio of inertial force to viscous force) will contribute to the intensification in heat diffusion in the blood flow. This will elevate temperatures via convective transport, despite the inhibiting effect of higher Prandtl number [51, 52].

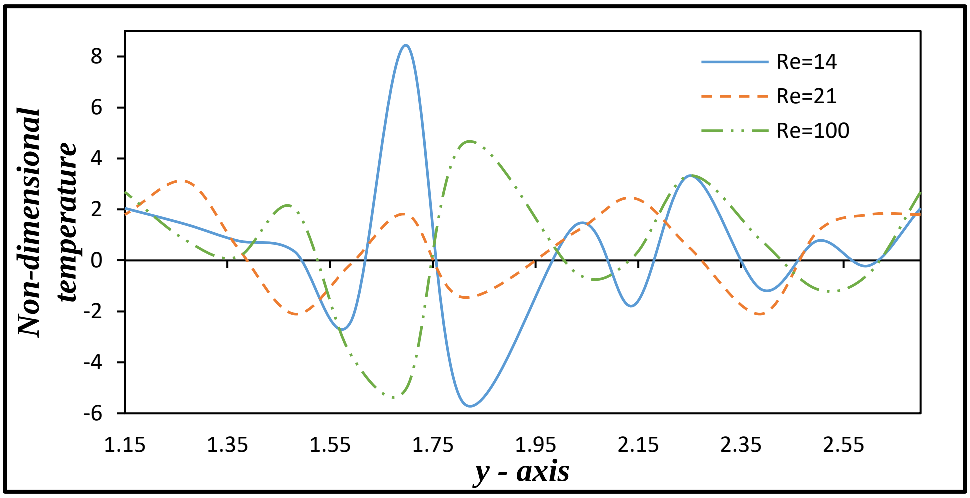

Figure 14 Effect of Reynolds number on temperature distribution at the prior outlet of the bifurcated arterial region for $Pr = 21, M = 0.6, t = 0.03, and\ x = 3.97$.

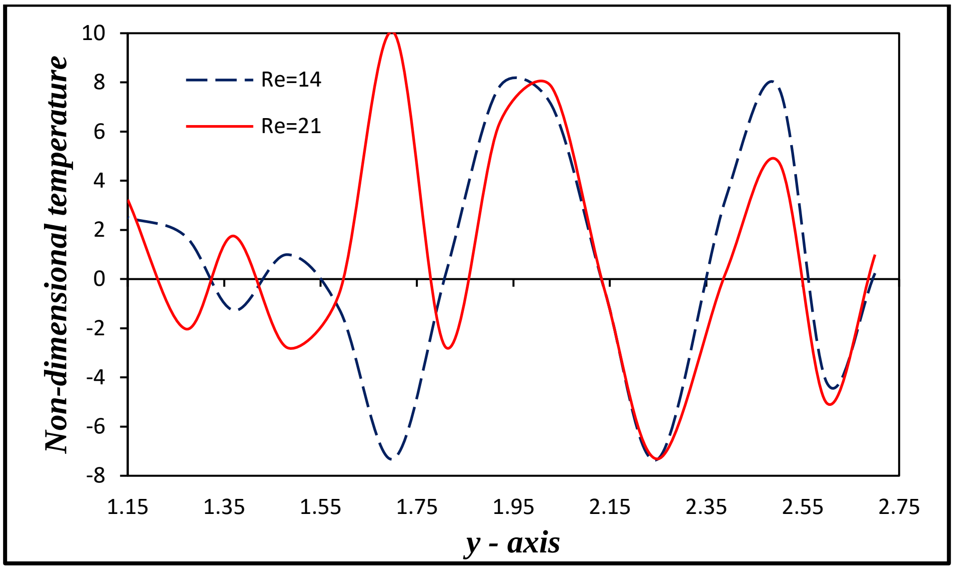

Figure 15 Effect of Reynolds number on temperature distribution at the prior outlet of the bifurcated arterial region for $Pr = 14, M = 0.6, t = 0.03, and x = 3.97$.

The **figures 14 and 15**, describes the temperature distribution at prior outlet for different values of Reynolds number and Prandtl number with *y*-coordinate (transverse) for a fixed location along the axial coordinate (x = 3.97). The above graphs show significant variation in the values of temperature with the various values of *Re and Pr*. Higher Reynolds number generally accentuates temperatures with *y* coordinate, although individual peaks do arise at lower Reynolds number. Lower magnitudes are again computed in Fig. 14 with increasing Prandtl number (*Pr* = *21*) compared with Fig. 15 (*Pr* = *14*). Additionally, it is evident from figures 11, 12, 14 and 15 that the temperature is significantly escalated from the inlet of the bifurcated artery for fixed values of time (t = 0.03). The oscillatory nature of the temperature field induced by pulsatile pressure gradient is clearly captured in these figures.

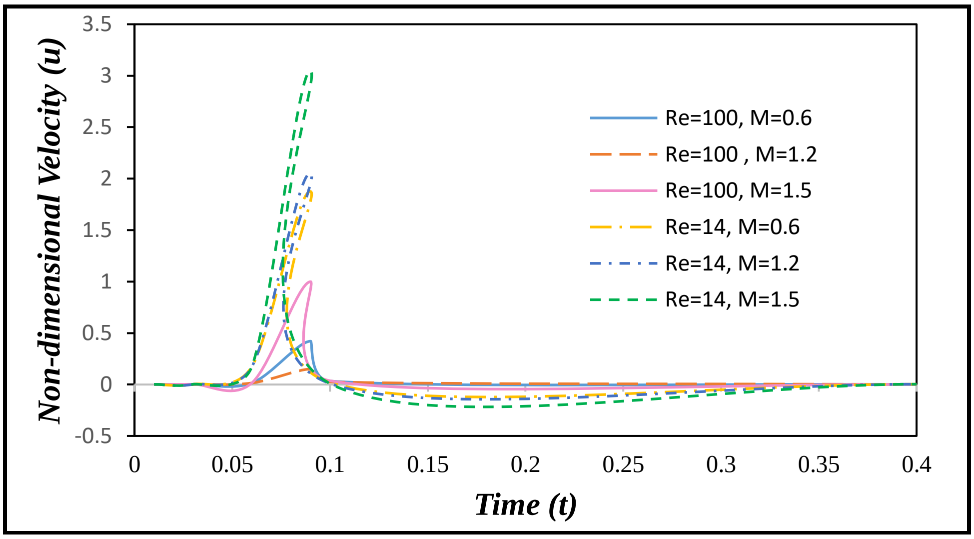

Figure 16 Effect of *M* on velocity distribution at saccular aneurysm region for $Pr = 21, x = 8.49$ and $y = 6.45$

The **figure 16** illustrates the response in velocity profiles for different values of Reynolds number and magnetic parameter (M) over time (t) at the saccular aneurysm. The curve shows the decrement in velocity with increment in Reynolds number and magnetic parameter (M). The increment in magnetic parameter (M), produced a corresponding elevation in Lorentzian hydromagnetic drag force which inhibits the fluid particles and decelerates the blood flow. The regulatory nature of external static magnetic field is therefore confirmed. A similar trend is computed in **Figure 17**, which shows significant decrement in velocity with an increase in the magnetic parameter (M)- velocity is minimized with stronger magnetic body force. For $M > 1$ the magnetic force exceeds the viscous force in the blood flow. The velocity profile topology is also warped with time progression evolving from a sharp increase at low times to an approximately linear decay with larger time elapse.

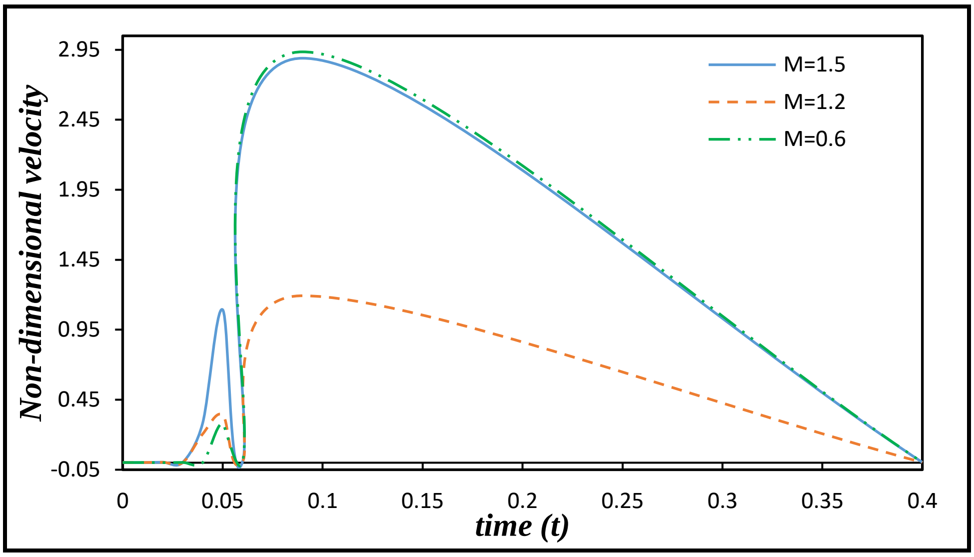

Figure 17 Effect of Magnetic parameter on velocity profile at saccular aneurysm arterial region for $Pr = 14, Re = 14, y = 6.45, and x = 8.49$.

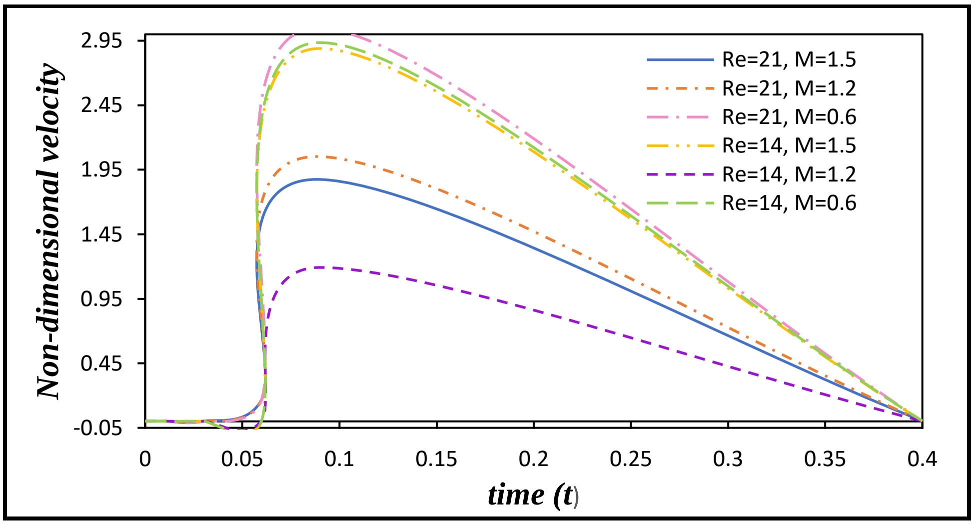

Figure 18 Effect of Reynolds number and magnetic parameter on velocity profile at saccular aneurysm region for $Pr = 14, y = 6.45, and\ x = 8.49$.

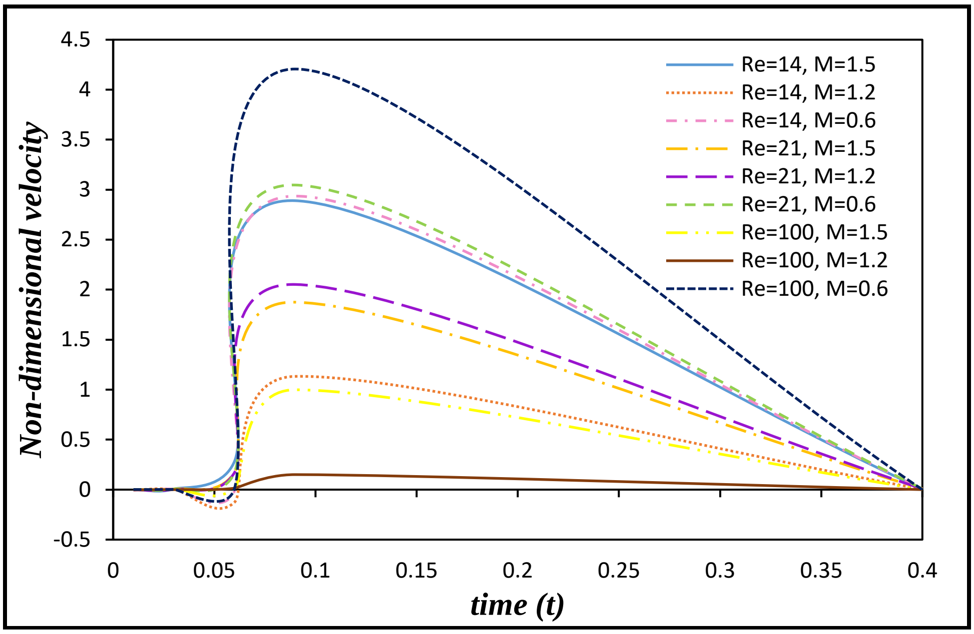

Figure 19 Effect of Reynolds number and magnetic parameter on velocity profile at peak of saccular aneurysm region for $Pr = 14, y = 6.42, and\ x = 7.70.$

Figures 18 and 19, depict the velocity evolution with respect to time for various values of Reynolds number and magnetic parameter at the saccular aneurysm and at outer wall of the saccular aneurysm respectively. The curves show a substantial decrement in velocity with an increment in Reynolds number. As noted earlier, Reynolds number quantifies the ratio of inertial (momentum) force to the viscous force. Due to the inertial forces dominating at higher *Re*, flow reversal is also induced near the outer wall. The additional effect of magnetic parameter is to damp the velocity field.

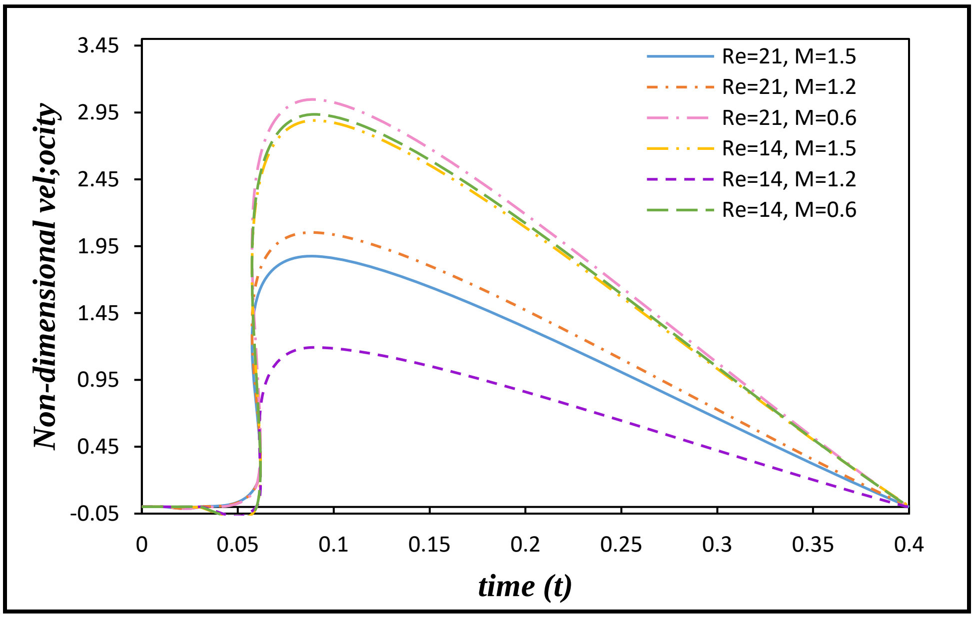

Figure 20 Effect of Reynolds number and magnetic parameter on velocity profile at saccular aneurysm region for $Pr = 14, y = 4.92, andx = 8.83$

Figure 20 portrays the velocity distribution with respect to time (*t*) for different values of Reynolds number and magnetic parameter (*M*) near the throat of the aneurysm prior to the outlet of the bifurcating artery. Similar to figures 18 and 19, there is a consistent depletion in velocity with increment in magnetic parameter (*M*), but also Reynolds number (*Re*). The dominant effect is the damping magnetic force which supercedes the inertial contribution from higher Reynolds numbers. Furthermore, the velocity remains largely invariant at the outer wall of the aneurysm and near the throat of aneurysm at a specific time instant (*t*=0.09).

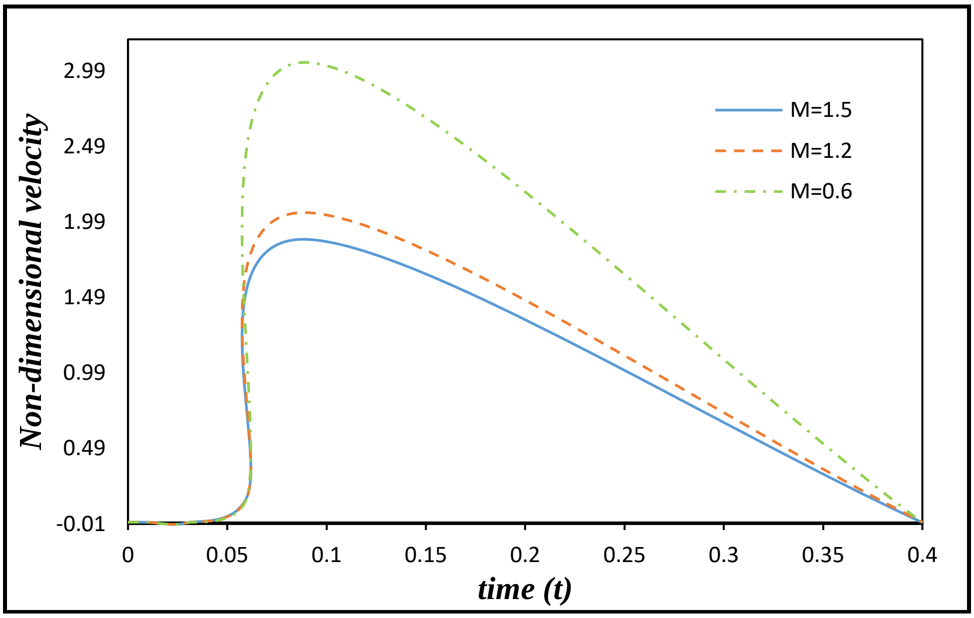

Figure 21 Effect of magnetic parameter on velocity profile at arterial bifurcation region for $Pr = 14, Re = 21, y = 6.37, and\ x = 9.95$.

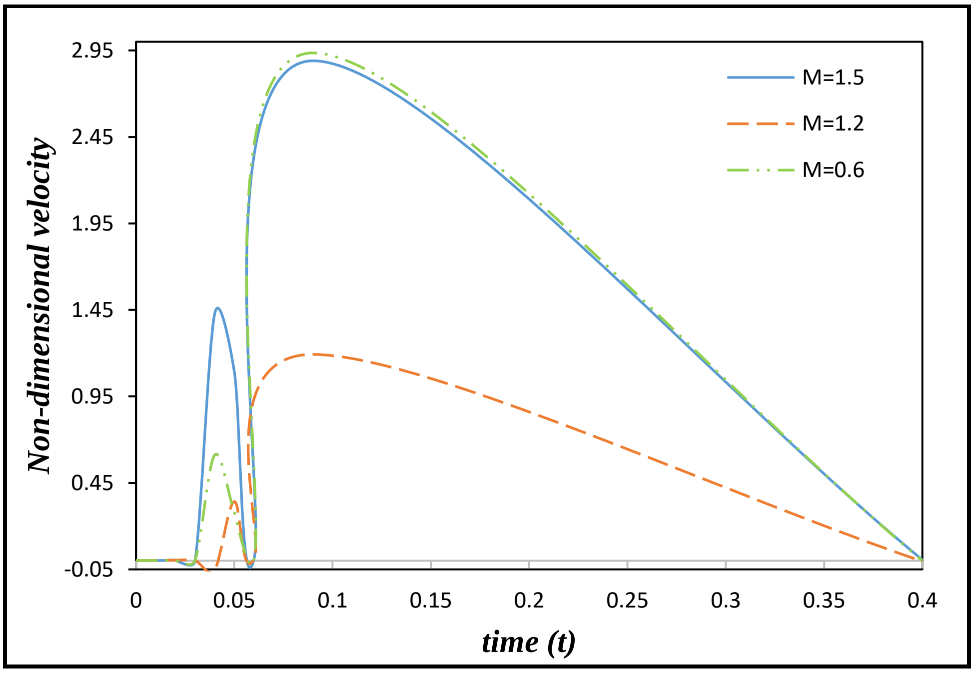

Figure 22 Effect of magnetic parameter on velocity profile at arterial bifurcation region for $Pr = 14, Re = 14, y = 4.92, and\ x = 8.83$.

Figures 21, 22 visualize velocity profiles with respect to time as magnetic parameter varies near both end locations of the aneurysm. The graphs indicate that velocity decreases with a rise in magnetic parameter (*M*) - it is reduced by in excess of 50% just by doubling the magnetic parameter (*M*). It is also evident that velocity changes more periodically at the throat of aneurysm in figure 22 in comparison to figure 21.

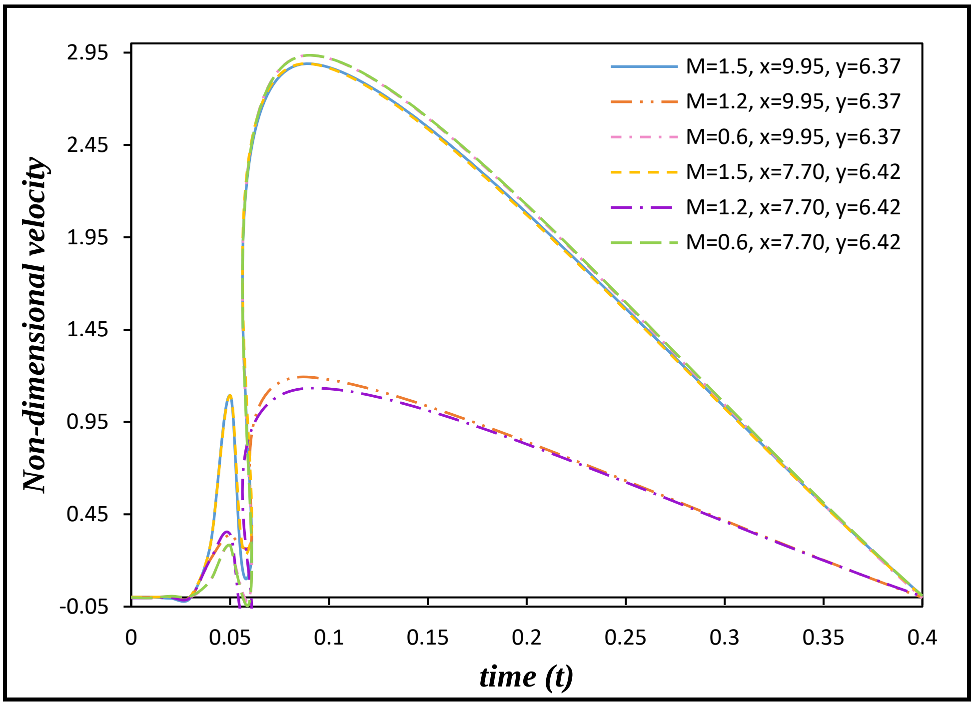

Figure 23 Effect of magnetic parameter on velocity profile at the throat of saccular aneurysm region and at peak of aneurysm for $Pr = 14, Re = 14$.

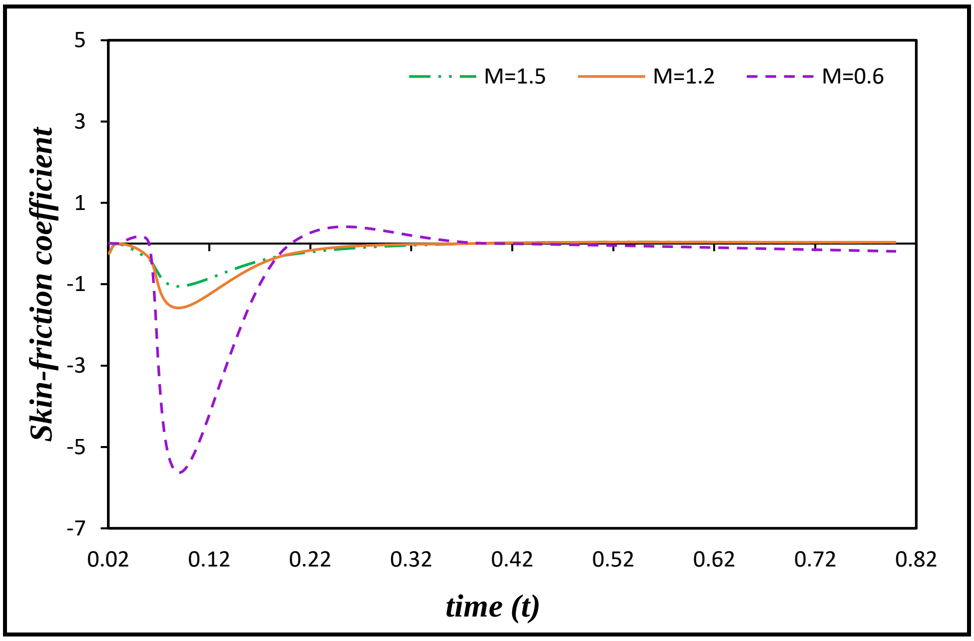

Figure 24 Effect of magnetic parameter (*M*) over skin-friction coefficient at saccular aneurysm region for $Re = 100, Pr = 21, y = 7.00 \text{ and } x = 8.52$.

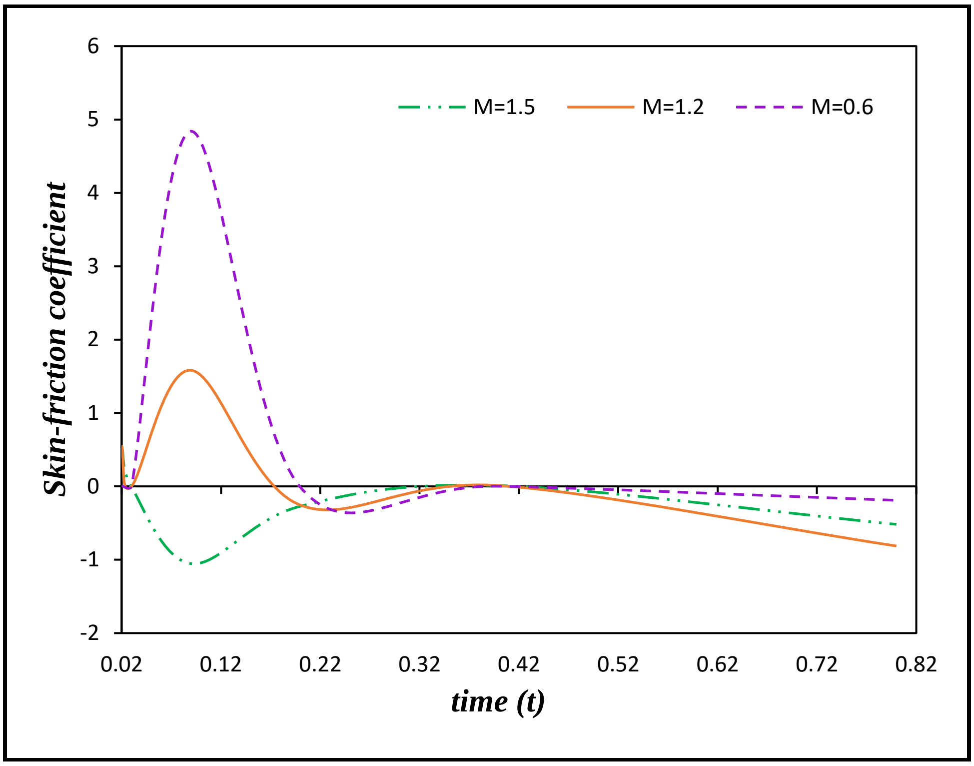

Figure 25 Effect of magnetic parameter (M) over skin-friction coefficient near bifurcation region for $Re = 100, Pr = 21, y = 2.79 \ and \ x = 8.60$.

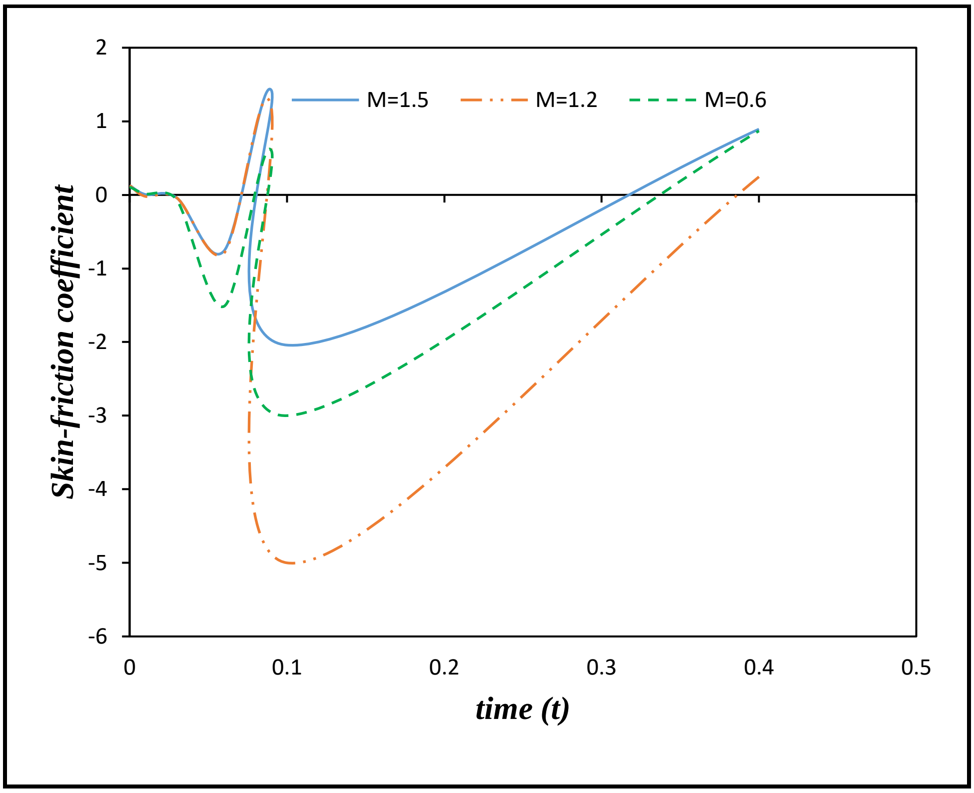

Figure 26 Effect of magnetic parameter (M) over skin-friction coefficient at saccular aneurysm region for$Re = 14, Pr = 21, y = 7.00 \ and \ x = 8.52$.

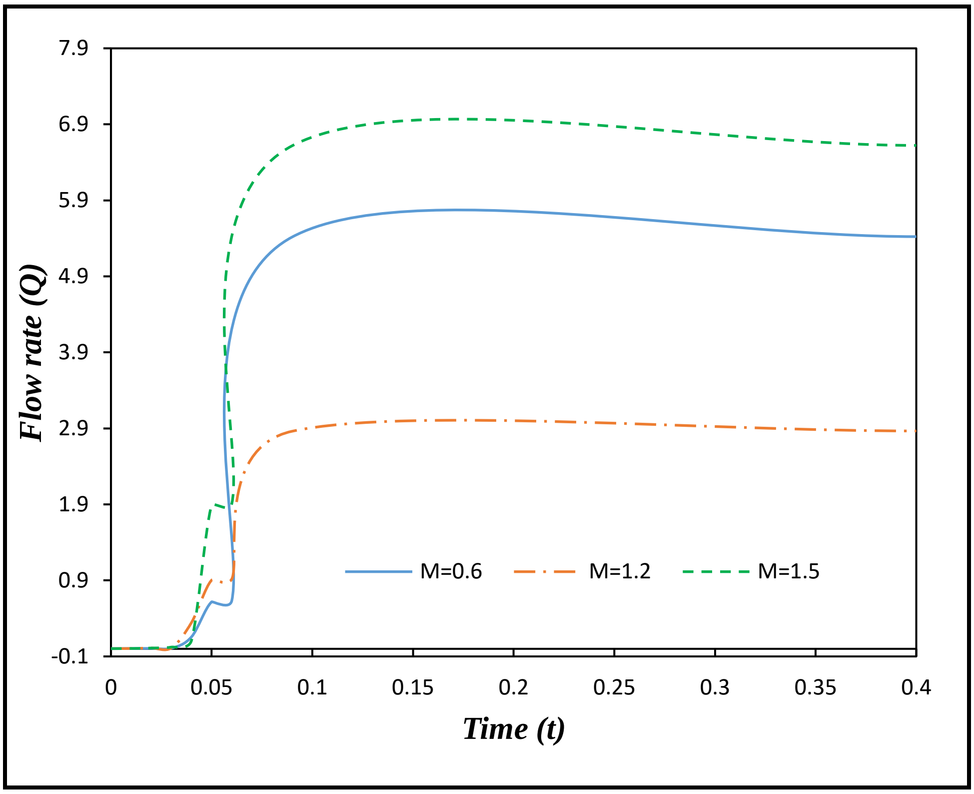

Figure 27 Effect of M on volumetric fluid flow rate at saccular aneurysm region for $Re = 14, Pr = 14, x = 8.15$ and $y = 6.45$.

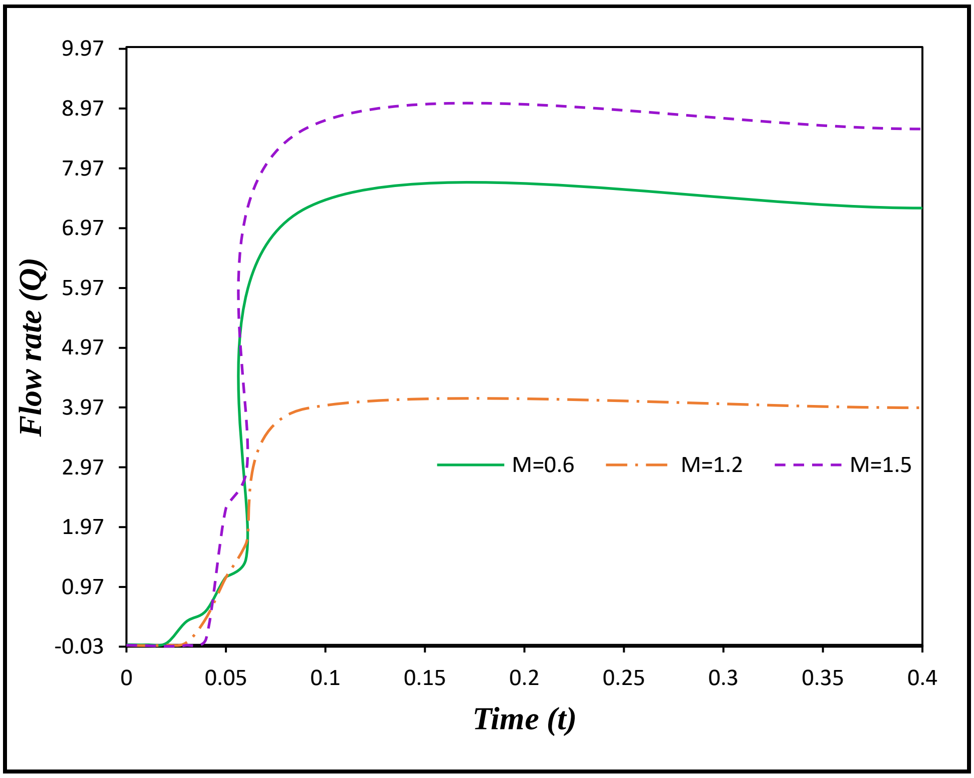

Figure 28 Effect of M on volumetric fluid flow rate near saccular aneurysm region for $Re = 14, Pr = 14, x = 10.0$ and $y = 6.45$.

Figure 23 presents the non-dimensional velocity evolution with time variation for three different values of magnetic parameter (*M*) *at two different points* along the aneurysm. The graph shows relatively little variation in the velocity at both the points at aneurysm wall; however, there is a strong decrease with the increment in magnetic parameter, *M*. Generally, all the velocity profiles are skewed to the left since the streaming blood is just passing through a region with flow recirculation along the outer wall side which pushes the fluid layers into the inner wall side of the artery. Hence, elevation in strength of magnetic field intensity (greater Hartmann number, *M*) additionally causes deceleration in the flow at the daughter branch.

Figures 24, 25 and 26, visualize the skin-friction coefficient evolution with variation in time (*t*) for three different values of magnetic parameter (*M*). Figures 24 and 26 describe the variation in skin-friction coefficient with decrement of Reynolds number (*Re=100 and Re=14*), respectively. The skin-friction coefficient (a representation of dimensionless wall shear stress, a key parameter in hemodynamics) shows some deviation from the velocity response (described earlier); whereas velocity is reduced with greater magnetic field effect, the skin friction is increased with an increment in magnetic parameter. However, the response to an increment in Reynolds number is similar to velocity distribution i. e. *it is reduced with greater magnetic effect*.

Finally Figures 27 and 28 present the volumetric fluid flow rate distributions with time variation at the outer wall of the aneurysm and near the aneurysm for $M = 0.6$, 1.2 and 1.5. Increment in magnetic parameter (*M*) causes enhancement in Lorentz force. This boosts the resistance to blood flow and manifests in a deceleration effect leading to a plummet in flow rate magnitudes. The excellent mechanism furnished by a non-intrusive magnetic field for regulating blood flow is therefore verified. The graph also shows that at a certain time instant ($t = 0.09$), the flow rate achieves a more constant topology at the saccular aneurysm due to bifurcations into the arterial branches.

6. CONCLUSIONS

In this study, motivated by providing a deeper insight into diseased cardiovascular flow dynamics, a finite element simulation of two dimensional magnetohydrodynamic heat conducting blood flow with coupled convective heat transfer through a bifurcated artery with a saccular (intercranial) aneurysm has been presented. The model generalizes previous studies by *amalgamating the Carreau-Yasuda model, heat transfer and magnetohydrodynamics with complex geometric features in realistic arterial hemodynamics with extensive visualization and interpretation. In previous studies these features have been considered separately and not simultaneously as in the current study.* Following transformation of the conservation equations for momentum and energy with associated boundary conditions, the resulting unsteady nonlinear non-dimensional boundary value problem has been solved with a variational commercial software, FREEFEM++. Validation with earlier studies has been included. Mesh independence tests have also been conducted. The 6-node Taylor-Hood triangular elements (P_2) have been deployed in the optimized mesh design. The effects of selected parameters (*magnetic body force parameter, Reynolds number and Prandtl number*) on velocity, temperature and hemodynamic pressure have been computed. The principal findings of the study may be crystallized as follows:

1. An increment in Reynolds number (*Re*) significantly decreases the pressure as well as velocity at saccular aneurysm.
2. The velocity shows a major decrement with growth in the magnetic parameter (*M*) at saccular aneurysm as well as near the throat of aneurysm (stronger Lorentzian magnetic drag force is produced with higher *M* values leading to flow deceleration).
3. The temperature distribution also shows a decrement at the parent artery (inlet) as well as at both the both distant and prior artery with enhancement in Prandtl number (*Pr*), due to reduction in thermal diffusivity relative to viscous diffusion rate.
4. The skin-friction coefficient shows the contrary behavior to that of velocity with increasing magnetic body force parameter i. e. skin friction is boosted with stronger magnetic field. However, with increment in Reynolds number, both velocity and skin friction are suppressed in magnitudes with some flow reversal arising.
5. The fluid flow rate also decreases with enhancement in magnetic parameter but tends to a near constant magnitude after a certain time elapse at the saccular aneurytic region.
6. Higher Reynolds number induces greater inertial effects in the blood flow, and creates recirculation zones with an associated depression in velocity at the outer wall of the artery.
7. Non-Newtonian (Carreau-Yasuda) fluid achieves higher velocity magnitudes than Newtonian fluids at intermediate times, but the reverse effect is computed at small times and high time values.

The present FREEFEM++ computations have revealed some interesting characteristics of saccular aneurysm and bifurcated arterial time-dependent hemodynamics for both Newtonian and non-Newtonian hydromagnetic blood flow and convective heat transfer. However only rigid wall geometries have been considered. It has delivered a greater insight of blood flow behavior in saccular aneurysm in the distal aortic artery which contains the aspects of novelty of the present study. Future studies may examine wall distensibility (fluid-structure interaction) and will be communicated imminently.

ACKNOWLEDGEMENTS

The authors are grateful to the Science and Engineering Research Board (SERB), Department of Science and Technology (DST), Government of India for undertaking the research work under the research project *File Number: ECR/2017/001053* dated 12/03/2018.

REFERENCES

[1]. Vasu, B., Dubey, A., & **Bég, O. Anwar** (2020). Finite element analysis of non-Newtonian magnetohemodynamic flow conveying nanoparticles through a stenosed coronary artery. *Heat Transfer-Asian Research*, *49*(1), 33-66.

[2]. Gupta, R., Mohan, I., & Narula, J. (2016). Trends in coronary heart disease epidemiology in India. *Annals of Global Health*, *82*(2), 307-315.

[3]. Davies, P. F. (2009). Hemodynamic shear stress and the endothelium in cardiovascular pathophysiology. *Nature clinical practice Cardiovascular medicine*, *6*(1), 16-26.

[4]. Baskurt, O. K., & Meiselman, H. J. (2003, October). Blood rheology and hemodynamics. In *Seminars in thrombosis and haemostasis* (Vol. 29, No. 5, pp. 435-450). New York: Stratton Intercontinental Medical Book Corporation, c1974-.

[5]. Baieth, H. A. (2008). Physical parameters of blood as a non-Newtonian fluid. *International journal of biomedical science: IJBS*, *4*(4), 323.

[6]. Amiri, M. H., Keshavarzi, A., Karimipour, A., Bahiraei, M., Goodarzi, M., & Esfahani, J. A. (2019). A 3-D numerical simulation of non-Newtonian blood flow through femoral artery bifurcation with a moderate arteriosclerosis: investigating Newtonian/non-Newtonian flow and its effects on elastic vessel walls. *Heat and Mass Transfer*, 55(7), 2037-2047.

[7]. Criminale, W. O., Jackson, T. L., & Joslin, R. D. (2018). *Theory and Computation in Hydrodynamic Stability*. Cambridge University Press.

[8]. Mathur, P., & Jain, S. (2013). Mathematical modeling of non-Newtonian blood flow through artery in the presence of stenosis. *Advances in Applied Mathematical Biosciences*, *4*(1), 1-12.

[9]. Tripathi, J., Vasu, B., & **Bég, O. Anwar** (2021). Computational simulations of hybrid mediated nano-hemodynamics (Ag-Au/Blood) through an irregular symmetric stenosis. *Computers in Biology and Medicine*, *130*, 104213.

[10]. Reddy, J. V. R., Srikanth, D., & Murthy, S. K. (2014). Mathematical modelling of couple stresses on fluid flow in constricted tapered artery in presence of slip velocity-effects of catheter. *Applied Mathematics and Mechanics*, *35*(8), 947-958.

[11]. Agrawal V, Paul C, Das M K and Muralidhar K (2015) Effect of coil embolization on blood flow through a saccular cerebral aneurysm. *Sadhana* 40(3): 875–887.

[12]. Chakravarty, S., & Sen, S. (2008). Analysis of pulsatile blood flow in constricted bifurcated arteries with vorticity-stream function approach. *Journal of medical engineering & technology*, *32*(1), 10-22.

[13]. Lou, Z., & Yang, W. J. (1992). Biofluid dynamics at arterial bifurcations. *Critical reviews in biomedical engineering*, *19*(6), 455-493.

[14]. Seo, T. (2013). Numerical simulations of blood flow in arterial bifurcation models. *Korea-Australia rheology journal*, *25*(3), 153-161.

[15]. Zhang, B., Jin, Y., Wang, X., Zeng, T., & Wang, L. (2017). Numerical simulation of transient blood flow through the left coronary artery with varying degrees of bifurcation angles. *Journal of Mechanics in Medicine and Biology*, *17*(01), 1750005.

[16]. Blanco, P.J., M.R. Pivello, R.A. Feijoo and S. Urquiza, 2007, Sensitivity of blood flow at the carotid artery to the heart inflow boundary condition, *3rd International Congress on Comput. Bioeng., Isla de Maragarita, Venezuela*, 1-6.

[17]. Dubey, A., Vasu, B., **Anwar Bég, O.,** Gorla, R. S., & Kadir, A. (2020). Computational fluid dynamic simulation of two-fluid non-Newtonian nanohemodynamics through a diseased artery with a stenosis and aneurysm. *Computer methods in biomechanics and biomedical engineering*, *23*(8), 345-371.

[18]. Jou, L.D. and S.A. Berger, 1998, Numerical simulation of the flow in the carotid bifurcation, *Theoret. Comput. Fluid Dynamics* **10**, 239-248.

[19]. Lee, S.W., L. Antiga, D. Spence and D.A. Steinman, 2008, Geometry of the carotid bifurcation predicts its exposure to disturbed flow, *Stroke AHAJ* **39**, 2341-2347.

[20]. Shaik, E., K.A. Hoffmann and J.F. Dietiker, 2006, Numerical flow simulations of blood in arteries, *4th AIAA Aerospace Science Meeting and Exhibit*, Reno, Nevada, USA, 294-307.

[21]. Valencia, Alvaro A., Amador M. Guzmán, Ender A. Finol, and Cristina H. Amon. (2006). Blood flow dynamics in saccular aneurysm models of the basilar artery. *ASME Journal of Biomechanical Engineering*, 128, no. 516-526.

[22]. Kumar, B. R., Yamaguchi, T., Liu, H., & Himeno, R. (2004). Blood flow in a vessel with asymmetric aneurysm. *International Journal of Applied Mechanics and Engineering*, *9*(3), 505-521.

[23]. Khan, M., & Hashim. (2015). Boundary layer flow and heat transfer to Carreau fluid over a nonlinear stretching sheet. *AIP Advances*, *5*(10), 107203.

[24]. Ali, N., Asghar, Z., Sajid, M., & **Bég, O. Anwar** (2019). Biological interactions between Carreau fluid and microswimmers in a complex wavy canal with MHD effects. *Journal of the Brazilian Society of Mechanical Sciences and Engineering*, *41*(10), 1-13.

[25]. Gireesha, B. J., Gorla, R. S. R., & Mahanthesh, B. (2015). Effect of suspended nanoparticles on three-dimensional MHD flow, heat and mass transfer of radiating Eyring-Powell fluid over a stretching sheet. *Journal of Nanofluids*, *4*(4), 474-484.

[26]. Mahanthesh, B., Shehzad, S. A., Ambreen, T., & Khan, S. U. (2020). Significance of Joule heating and viscous heating on heat transport of MoS 2–Ag hybrid nanofluid past an isothermal wedge. *Journal of Thermal Analysis and Calorimetry*, 1-9.

[27]. Mahanthesh, B., Shashikumar, N. S., & Lorenzini, G. (2020). Heat transfer enhancement due to nanoparticles, magnetic field, thermal and exponential space-dependent heat source aspects in nanoliquid flow past a stretchable spinning disk. *Journal of Thermal Analysis and Calorimetry*, 1-9.

[28]. Mahanthesh, B., Gireesha, B. J., & Gorla, R. S. R. (2017). Unsteady three-dimensional MHD flow of a nano Eyring-Powell fluid past a convectively heated stretching sheet in the presence of thermal radiation, viscous dissipation and Joule heating. *Journal of the Association of Arab Universities for Basic and Applied Sciences*, *23*, 75-84.

[29]. Sreedevi, P., Reddy, P. S., & Chamkha, A. J. (2018). Magneto-hydrodynamics heat and mass transfer analysis of single and multi-wall carbon nanotubes over vertical cone with convective boundary condition. *International journal of Mechanical sciences*, *135*, 646-655.

[30]. Sreedevi, P., & Reddy, P. S. (2019). Effect of SWCNTs and MWCNTs Maxwell MHD nanofluid flow between two stretchable rotating disks under convective boundary conditions. *Heat Transfer—Asian Research*, *48*(8), 4105-4132.

[31]. Reddy, P. S. A., & Chamkha, A. (2018). Heat and mass transfer characteristics of MHD three-dimensional flow over a stretching sheet filled with water-based alumina nanofluid. *International Journal of Numerical Methods for Heat & Fluid Flow*.

[32]. Nadeem, S., Ijaz, S., & Adil Sadiq, M. (2014). Inspiration of induced magnetic field on a blood flow of Prandtl nanofluid model with stenosis. *Current Nanoscience, 10*(5), 753-765.

[33]. Mekheimer, K. S. (2008). Effect of the induced magnetic field on peristaltic flow of a couple stress fluid. *Physics Letters A*, *372*(23), 4271-4278.

[34]. Mekheimer, K. S., & El Kot, M. A. (2008). Influence of magnetic field and Hall currents on blood flow through a stenotic artery. *Applied Mathematics and Mechanics*, *29*(8), 1093.

[35]. Ponalagusamy, R., & Selvi, R. T. (2015). Influence of magnetic field and heat transfer on two-phase fluid model for oscillatory blood flow in an arterial stenosis. *Meccanica*, *50*(4), 927-943.

[36]. Ponalagusamy, R., & Priyadharshini, S. (2018). Numerical investigation on two-fluid model (micropolar-Newtonian) for pulsatile flow of blood in a tapered arterial stenosis with radially variable magnetic field and core fluid viscosity. *Computational and Applied Mathematics*, *37*(1), 719-743.

[37]. Reddy, P. S., Jyothi, K., & Reddy, M. S. (2018). Flow and heat transfer analysis of carbon nanotubes-based Maxwell nanofluid flow driven by rotating stretchable disks with thermal radiation. *Journal of the Brazilian Society of Mechanical Sciences and Engineering*, *40*(12), 1-16.

[38]. Reddy, P. S., Sreedevi, P., Chamkha, A. J., & Al-Mudhaf, A. F. (2018). Heat and mass transfer boundary-layer flow over a vertical cone through porous media filled with a cu–water and ag–water nanofluid. *Heat Transfer Research*, *49*(2).

[39]. Sreedevi, P., Reddy, P. S., & Sheremet, M. (2019). A comparative study of Al2O3 and TiO2 nanofluid flow over a wedge with non-linear thermal radiation. *International Journal of Numerical Methods for Heat & Fluid Flow*.

[40]. Rajashekhar, C., Manjunatha G., and Fabian B., Finite element simulation of blood flow through an artery bifurcation: a mathematical model, *Malaysian Journal of Mathematical Sciences* **11**, no. 2: 165-179, 2017.

[41]. Rehman, K. U., Al-Mdallal, Q. M., Tlili, I., & Malik, M. Y. (2020). Impact of heated triangular ribs on hydrodynamic forces in a rectangular domain with heated elliptic cylinder: finite element analysis. *International Communications in Heat and Mass Transfer*, *112*, 104501.

[42]. Rehman, K. U., Malik, M. Y., Al-Mdallal, Q. M., & Al-Kouz, W. (2020). Heat transfer analysis on buoyantly convective non-Newtonian stream in a hexagonal enclosure rooted with T-Shaped flipper: hybrid meshed analysis. *Case Studies in Thermal Engineering*, *21*, 100725.

[43]. Rehman, K. U., Al-Kouz, W., Sherif, E. S. M., & Abdelmalek, Z. (2020). Hybrid meshed analysis on rhombus shaped solid material domain (RSSMD) equipped with non-Newtonian liquid stream. *Journal of Science: Advanced Materials and Devices*, *5*(4), 476-486.

[44]. Rehman, K. U., Malik, M. Y., Al-Kouz, W., & Abdelmalek, Z. (2020). Heat transfer individualities due to evenly heated T-Shaped blade rooted in trapezium enclosure: Numerical analysis. *Case Studies in Thermal Engineering*, *22*, 100778.

[45]. Zahri, M., Al-Kouz, W., Rehman, K. U., & Malik, M. Y. (2020). Thermally magnetized rectangular chamber optimization (TMRCO) of partially heated continuous stream: Hybrid meshed case study. *Case Studies in Thermal Engineering*, *22*, 100770.

[46]. Werner, C., & Gorla, R. S. R. (2013). Probabilistic study of bone remodeling using finite element analysis. *International Journal of Applied Mechanics and Engineering*, *18*(3), 911-921.

[47]. Srinivasacharya, D., & Rao, G. M. (2016). Mathematical model for blood flow through a bifurcated artery using couple stress fluid. *Mathematical biosciences*, *278*, 37-47.

[48]. Zain, N. M., & Ismail, Z. (2019). Hartmann and Reynolds Numbers Effects in the Newtonian Blood Flow of a Bifurcated Artery with an Overlapping Stenosis. *MATEMATIKA: Malaysian Journal of Industrial and Applied Mathematics*, *35*(2), 213-227.

[49]. Victor, S. A., & Shah, V. L. (1975). Heat transfer to blood flowing in a tube. *Biorheology*, *12*(6), 361-368.

[50]. Çinar, Y., Şenyol, A. M., & Duman, K. (2001). Blood viscosity and blood pressure: role of temperature and hyperglycemia. *American Journal of Hypertension*, *14*(5), 433-438.

[51]. Barozzi, G. S., & Dumas, A. (1991). Convective heat transfer coefficients in the circulation. *ASME Journal of Biomechanical engineering*, *113*(3), 308-313.

[52]. Victor, S. A., & Shah, V. L. (1976). Steady state heat transfer to blood flowing in the entrance region of a tube. *International Journal of Heat and Mass Transfer*, *19*(7), 777-783.